Research Square

Preprints are preliminary reports that have not undergone peer review.
They should not be considered conclusive, used to inform clinical practice,
or referenced by the media as validated information.

Climatic and ice dynamic controls on the deglaciation of the Laurentide Ice Sheet

Samuel Chester

schester@ldeo.columbia.edu

Columbia University https://orcid.org/0009-0009-6195-9040

Jacqueline Austermann

Columbia University

Benjamin Stoker

Columbia University

Roger Creel

Texas A&M University

William D'Andrea

Columbia University

Blake Dyer

University of Victoria

Nicolas Young

Columbia University

April Dalton

Woodwell Climate Research Center

Research Article

Keywords: Ice Sheets, Cryosphere, Paleoclimate, Laurentide

Posted Date: November 10th, 2026

DOI: https://doi.org/10.21203/rs.3.rs-11651693/v1

License: This work is licensed under a Creative Commons Attribution 4.0 International License.
Read Full License

Additional Declarations: The authors declare no competing interests.

Climatic and ice dynamic controls on the deglaciation of the Laurentide Ice Sheet

Samuel J. Chester[1*], Jacqueline Austermann[1], Benjamin J. Stoker[1], Roger C. Creel[2], William J. D'Andrea[1], Blake Dyer[3], Nicolás E. Young[1], April S. Dalton[4]

[1]Lamont-Doherty Earth Observatory, Columbia University, Palisades, NY 10964, USA

[2]Department of Geology & Geophysics, Texas A&M University, College Station, TX 77843, USA.

[3]School of Earth and Ocean Sciences, University of Victoria, Victoria V8P 5C2, Canada.

[4]Woodwell Climate Research Center, Falmouth, MA 02540, U.S.A.

[*]Corresponding author. Email: schester@ldeo.columbia.edu

Ice sheets respond to both external climatic forcings and dynamic processes related to ice flow, basal sliding, marine instabilities, and solid-Earth interactions, yet the relative importance of these controls is unclear. Here, we investigate the role of these drivers during the last deglaciation of the Laurentide Ice Sheet (LIS). To overcome an incomplete chronology of the deglaciation, we use Bayesian data assimilation to reconstruct retreat of the LIS since the Last Glacial Maximum (26 to 19 ka) as a continuous spatiotemporal field with quantified uncertainty by integrating geochronologic and geomorphic constraints with an ensemble of physics-based ice-sheet models. Our reconstruction shows a complex and asynchronous pattern of deglaciation. At continental scale, average retreat rates align with hemispheric climate change, however, on a regional scale we find that the rate of deglaciation was spatially and temporally variable. Our reconstruction allows for a novel comparison to proxies of mechanical controls on deglaciation that reveals regional retreat was closely aligned with the extent of soft sediment

underlying ice-sheet margins, the degree of ice streaming, and the presence of proglacial lakes. These mechanical controls explain rapid retreat in places that appear out of sync with climate changes. Based on these results, we identify basal sliding and dynamic discharge as critical controls on large ice-sheet collapse and propose that internal feedbacks will strongly influence the response of the world's modern ice sheets to atmospheric and ocean warming.

1 Introduction

The collapse of the Laurentide Ice Sheet (LIS), the world's largest ice mass at the Last Glacial Maximum (LGM; 26-19 thousand years ago, ka), represents a case study in the response of a continental-scale ice sheet to global climate change. The underlying driver of melting over the last glacial termination is related to external climate forcings, including insolation, atmospheric greenhouse gas concentration, and ocean and atmospheric temperatures (*1, 2*); however, with respect to these forcings, there is evidence for both in- (*3–5*) and out-of-phase (*6–9*) response of the LIS. This asynchronous behavior challenges the hypothesis that the rates of deglaciation were controlled primarily by Northern Hemisphere climate changes. Furthermore, transient climate modeling suggests that LIS surface mass balance was mostly positive through the initial deglaciation, indicating that to trigger and sustain early ice loss, other processes in addition to climate forcing are necessary (*10, 11*).

A number of properties at the ice-bed interface can influence patterns of deglaciation by modulating basal sliding and ice flow and have been proposed as important controls on LIS retreat (*12–17*). While basal properties affect all grounded ice, they are particularly important in the development of ice streams, which arise from a positive feedback between enhanced basal velocity and frictional heating at the bed (*18–20*). In modern ice sheets and paleo ice-sheet simulations, ice streaming drives rapid discharge and upstream thinning (*21–23*). Because ice streaming as a result of basal properties can facilitate non-linear responses to climate forcings, it offers a possible mechanism to explain the complex relationships between LIS retreat and climate change observed over the deglaciation. Other non-linear feedback mechanisms, including ice saddle collapse, calving into proglacial lakes, and isostatic adjustment, may have further destabilized the LIS during deglacia-

tion (*1, 11, 24–26*). Parsing the relative roles of climate forcing and mechanical processes in LIS deglaciation is critical for understanding glacial-interglacial cycles, Pleistocene climate evolution, and the (in)stability of the world's remaining ice sheets under continued warming.

Constraining the precise timing of ice retreat and quantifying chronological uncertainties is critical to disentangle the drivers of LIS deglaciation (*2*). LIS reconstructions have typically relied on expert judgment to combine geomorphic observations with geochronological constraints to map ice margin positions at discrete time slices (*9, 27–29*). Mapping is advantageous because it combines many data types—geochronological, geomorphic, and geologic—and provides detailed margin geometry where data are available. However, this approach also poses challenges. First, hand-mapped reconstructions are limited to time slices, which require the projection of chronological constraints onto discrete time intervals, introducing additional uncertainty. Second, while data-dense regions can provide retreat rates along one-dimensional transects, deriving spatially continuous retreat rates across an entire ice sheet is challenging. Moreover, it is difficult to compare time slice reconstructions to spatially or temporally continuous datasets such as surficial geology or global temperature. Finally, geochronological constraints are usually sparse, unevenly distributed, noisy, and sometimes conflicting, thereby necessitating subjective decisions about margin position. Quantifying the uncertainty in margin position that stems from these decisions (and the underlying data) is thus challenging. Because of this difficulty, such reconstructions commonly rely on qualitative descriptions or minimum-maximum positions to represent confidence [e.g. (*9, 30, 31*)].

Glaciological modeling offers alternative approaches to reconstruct past ice sheets, either by inverting paleo sea-level data for ice-sheet extent and thickness through glacial isostatic adjustment (GIA) modeling, or through physics-based, climate-forced forward modeling of ice dynamics [e.g. (*32, 33*)]. These approaches are advantageous because they incorporate additional constraints—including sea-level data, paleoclimate forcings, and ice-flow thermodynamics—and can produce spatiotemporally continuous reconstructions of both ice extent and thickness. However, models also introduce sources of uncertainty and inaccuracy due to imperfectly constrained inputs (e.g. mantle viscosity, climatic forcings) and physical processes (e.g. basal sliding laws, calving dynamics). As a result, current physics-based ice sheet models don't reproduce mapped margin chronologies on a continental scale (*34*). Additionally, existing GIA-based ice sheet reconstructions do not offer independent estimates of ice margin retreat because they commonly use mapped ice margin

chronologies as inputs [e.g. (*32, 35*)].

We address these limitations by developing a new approach to reconstruct the deglacial history of the LIS margin using Bayesian data-model assimilation. Data assimilation offers a solution for inferring complete spatiotemporal fields with quantified uncertainty from noisy and/or spatially-limited proxy datasets (*36*). Statistical approaches to data assimilation use model estimates as a starting point (the prior) and update these predictions using data constraints to infer the range of most likely scenarios (the posterior). Bayesian techniques have previously been used to study linear transects of ice margin retreat or thinning (*8, 20, 24*); however, until now these approaches have included only geochronological constraints, have been limited to one dimension, and have incorporated limited prior information (e.g. the directionality of retreat). Here, we extend the principles of this approach to the entire LIS, inferring a space-time deglaciation field from data across North America by merging prior information from ice sheet models with geomorphic and geochronologic constraints on margin geometry. The resulting data-model Assimilation-based Laurentide Ice Sheet deglacial reconstruction (ALIS) offers a spatio-temporally continuous picture of ice margin retreat with quantified uncertainties and allows us to test hypotheses about the drivers of LIS deglaciation during the last termination.

In brief, the ALIS reconstruction uses a hierarchical Bayesian framework to infer a posterior distribution of deglaciation time for the LIS by assimilating geochronologic and geomorphic data with an ensemble of ice sheet reconstructions (see section 4). The geochronologic constraints are from a recent North American compilation (*9*)—updated to include recent publications (*37–43*)—that includes ^{10}Be terrestrial cosmogenic nuclide (TCN) ages and calibrated radiocarbon ages, representing direct and age-limiting constraints on margin position, respectively (see section 4; Fig. 1). We supplement these ages with a dataset of mapped moraines and paleo ice streams that constrain margin geometry and retreat direction (*9, 44*). We focus primarily on the LIS and exclude data associated with the Cordilleran Ice Sheet (CIS) except for a subset of CIS data west of the CIS-LIS saddle to capture the unzipping of the ice-free corridor (Fig. 1). For the ice sheet reconstructions, we use a seven-member ice sheet ensemble that reflects a diverse range of possible retreat scenarios (see section 4). The reconstructions are weighted based on their fit to the data; consequently, in data-poor regions, rather than simply interpolating between locations, the posterior mean tends towards the learned (best-fit) ensemble prediction while still acknowledging the lack of

constraints via high posterior uncertainty. The resolution of the ALIS reconstruction is controlled by the length-scales of covariance in the data (see section 4) and can therefore be thought of as providing the simplest, or smoothest, reconstruction given the constraints. Topography is not incorporated as information in the model, and thus, we expect to infer margins that are relatively smooth rather than confined by topographic features. Finally, we note that given this formulation (see section 4), the ALIS can only capture the last time of deglaciation from a given location and cannot reproduce the build-up to the LGM extent or local readvances.

2 Results

2.1 Patterns of retreat

Our ALIS reconstruction reveals a complex pattern of deglaciation (Fig. 2). Along the southern margin, where terrestrial data are available and the posterior uncertainties are well constrained, the ALIS shows highly asynchronous retreat from the Last Glacial Maximum Extent (LGME), ranging from $\sim$ 26 to 16 ka with the earliest deglaciation beginning along the US Atlantic coast and latest retreat occurring near the James and Des Moine Lobes. Broadly, the Atlantic side of the LIS is characterized by slow initial retreat; in the northern sectors, this pace continues throughout the deglaciation (e.g. Baffin Island, eastern Labrador), while to the south, periods of accelerated deglaciation occur associated with the deglaciation of the St. Lawrence Channel ($\sim 20 - 14$ ka), the separation and collapse of the Newfoundland ice dome ($\sim 15 - 13$ ka), and the migration of the margin across Maine and Nova Scotia ($\sim 19 - 14$ ka).

The continental Keewatin and Great Lakes sectors of the LIS show a markedly different pattern of initial deglaciation. While the model cannot resolve episodic retreat and readvance that may have occurred before achieving the maximum extent [e.g. (*3*)], the final deglaciation age is notably later by up many thousands of years compared to the northeast US, for example near Long Island. Following this relatively late withdrawal from the LGME around 16 ka, ice margins in the western Great Lakes sector rapidly retreat northward, broadly synchronous with the separation of the LIS and CIS and the development of the ice-free corridor. In the south, the corridor begins to open slowly at 17.4 ka (posterior median, 18.6-16.4 ka 95% CI), while in the north it opens later (15.6

ka; 16.1-15.0 ka 95% CI) and proceeds faster (Fig. S9). A fully ice-free corridor is achieved at 14.4 ka (14.9-13.8 ka 95% CI). This timing corresponds (within uncertainty) with the inferred age of CIS-LIS saddle collapse from ice sheet modeling, the onset of the warm Bølling–Allerød (BA; 14.7-12.9 ka), and the rise in global mean sea level of Meltwater Pulse 1A (*24, 45–47*).

The later stages of LIS deglaciation are characterized by the breakup of the Keewatin, Labrador, and Foxe ice domes. As the Hudson Strait ice stream retreats, the Foxe sector separates from the southern domes, and its southern ice margin rapidly retreats northward. Next, the Hudson Bay saddle collapses, separating the Keewatin and Labrador sectors (8.5 ka median; 9.2-8.0 ka 95% CI) overlapping within uncertainty with the 8.2 ka climate event [8.5-8.0 ka; (*48, 49*)]. The Keewatin dome disappears by 7.5 ka (8.4-6.9 ka 95% CI), followed by the Labrador (7.1 ka median; 7.9-6.4 ka 95% CI), coincident with the Holocene Thermal Maximum (*50*). Finally, the Foxe dome shrinks to become the Barnes Ice Cap, the last vestige of the LIS (*43, 51*).

2.2 Uncertainty quantification

The data-assimilation approach offers a novel method for uncertainty quantification in paleo margin position. Uncertainties in the ALIS reconstruction—represented by 95% posterior credible intervals (CI)—are spatially variable and influenced by the density, quality, and type (i.e., direct or limiting) of geochronological constraints, as well as the imposed spatial covariance structure (see section 4). Regions of high data density, particularly TCN ages and dated moraines, have lower posterior uncertainty; for example, the US Northeast (New Jersey, New York and New England), the US Midwest, and eastern Baffin Island. Regions with large posterior uncertainty highlight areas for potential future data collection, in particular, the LGME margin, which is unconstrained (> 3 thousand years, kyr, 95% CI) across marine based sectors and in Montana, US, where data are sparse and mostly limiting. Some core interior regions—e.g. Keewatin Dome and Hudson Bay Lowlands—also show high posterior uncertainty ($\sim$ 1.5 – 3 kyr, 95% CI) reflecting TCN data sparsity.

2.3 Spatially variable retreat rates

Because the ALIS reconstruction provides a spatially and temporally continuous field of deglaciation, it enables derivation of metrics that cannot be obtained from traditional time-slice reconstructions. For example, previous approaches that estimated retreat rates along individual transects using linear interpolation between mapped margin positions or projected ages onto a transect cannot fully consider changes in the geometry of the margin with time. Using ALIS, we can estimate ice margin position and retreat rate directly from the deglaciation field (Fig. 2C; Fig. S8) to develop regional and ice-sheet-scale time series' of average retreat rate (RR) and rate of area loss (RAL) (Fig. 3).

At an ice-sheet scale, RR and RAL accelerate following the onset of deglaciation ($\sim$ 25 ka), reach maximum values around 14.5 ka, then slow throughout the warm BA (14.6-12.9 ka) and cold Younger Dryas [YD; 12.9-11.7 ka] climate intervals Fig. 3; (*47, 52, 53*)]. Near the transition to the Holocene (11.7 ka), retreat accelerates, culminating in a second pulse around 8.5 ka. This ice-sheet average, however, conceals a regionally asynchronous pattern of ice-margin retreat. Decomposing ALIS into regional sectors (Fig. 4), we find that the early deglaciation ($\sim$25 to 22 ka) occurs mainly on the southeast Atlantic coastline. Acceleration in RR from $\sim$22-15 ka is driven by a cascade of ice loss, first in the Atlantic and Great Lakes regions and then in the western Keewatin sector. Through the BA (warm) and YD (cold), RR and RAL slow in the Keewatin, Great Lakes, and Atlantic sectors, while retreat gradually accelerates in the Hudson Bay, Labrador, and Foxe sectors. A second pulse of LIS retreat in the Holocene is characterized by recession of the Hudson Bay Ice Stream, collapse of the Hudson Bay saddle, and the subsequent asynchronous demise of the Foxe and Labrador ice domes. Sensitivity tests show that this asynchronous behavior is observed across different regional delineations (Fig. S1)

2.4 LIS margin conditions and mechanical controls on deglaciation

The ALIS reconstruction allows us to assess conditions related to ice dynamics along the active margin (the edge of the LIS at a given time), which provides context for how mechanical processes might have influenced deglaciation. These include basal conditions (surficial sediment thickness and type), the number of active ice streams, and the proportion of the margin that is lake-terminating [see section 4; (*25, 54, 55*)]. At the continental scale, average sediment thickness along the margin

is generally high during initial deglaciation with a peak during the BA, after which it decreases through the end of the YD (Fig. 3F). After the YD, average sediment thickness rises again, peaking just before the collapse of the Hudson Bay saddle, and then decreases through the final deglaciation.

As an alternative method to assess basal conditions along the LIS margin through time, we compare the ALIS reconstruction to maps that classify North America by sediment type (silt, clay, or sand), the percentage of sediment cover (continuous, discontinuous, or no sediment), and the bedrock geology (sedimentary and non-sedimentary units) [for details on the classifications see (*54*)]. For each map type, we calculate the proportion of the margin in each category; Fig. 3H shows categories that reflect soft, deformable sediment: silt, continuous sediment cover, and sedimentary bedrock. During initial deglaciation, the proportion of the margin overlaying fine-grained silty sediment, and sedimentary bedrock is high (80-100%) and then decreases from around 15 ka until ~10 ka when it starts to increase, preceding Hudson Bay saddle collapse (Fig. 3H, red and orange lines). The proportion of the margin overlaying continuous sediment cover closely resembles average sediment thickness, with the margin mostly occupying continuous deposits in the early stages, followed by a decrease to less than 50% at the end of the YD (Fig. 3H, green line). It then increases, reaching a maximum at Hudson Bay saddle collapse coincident with average sediment thickness, RR, and RAL (Fig. 3E, F, and G).

Ice streaming, quantified as the number of possible active ice streams at a given time (see section 4), increases from the very early deglaciation until the BA (~ 25 ka to ~ 15 ka), and then declines until the mid-Holocene, interrupted by a brief period of stability at ~10 ka when several streams south of Hudson Bay overlying thick sedimentary deposits are activated preceding saddle collapse (Fig. S8). The ice sheet also becomes increasingly lake-terminating throughout initial deglaciation, peaking during the BA (Fig. 3J) before declining sharply through the YD. Subsequently, a smaller proportion of the margin is lake terminating through the early Holocene until again declining sharply before the 8.2 ka event, which aligns with the draining of Lake Agassiz-Ojibway (*56*).

The correlation among ice-streaming, sediment thickness at the margin, pro-glacial lake termination, and the inferred RAL and RR is weak at the continental scale; however, regionally, we find remarkable alignment throughout deglaciation of the LIS (Fig. 5). In many regions, the acceleration of ice loss is concordant with or slightly lags the increase in average sediment thickness and the activation of ice streams, with the notable exception of marine-terminating streams early in the

deglaciation (discussed below in 3.3). Similarly, intervals of slowing retreat rates correspond to thinner or less sediment cover at the base of ice margins, as well as with reduced ice streaming. For the central terrestrial sectors of LIS—the Great Lakes, Hudson Bay, and Keewatin—proglacial lake density also increases during major pulses of deglaciation (Fig. 5).

3 Discussion

3.1 ALIS: a new reconstruction and tool

The ALIS reconstruction is generally consistent with a previous reconstruction built on the same geochronological and geomorphic database: the North American Deglacial Isochrones [NADI-1; (*9*)], though with quantified uncertainties. Discrepancies primarily result from differences in the treatment of radiocarbon ages, which are here modeled conservatively and explicitly as minimum-limiting data. This treatment allows for earlier deglaciation particularly in Manitoba, the Canadian Arctic Archipelago, and the Quebec-Labrador sector (see section 4; Fig. S7). Other discrepancies arise from resolution differences; the coarser ALIS reconstruction cannot resolve smaller ice streams and outlet glaciers in the NADI-1 reconstruction. Also, geomorphic evidence used in the NADI-1 reconstruction—including flow sets, eskers and striations—result in some differences, for example the location of smaller ice masses during the final collapse of the Labrador dome. Finally, local readvances cannot be resolved in the ALIS reconstruction and thus the posterior may show a bias towards 'slow retreat' in locations where a readvance actually occurred. A detailed discussion of these discrepancies is provided in the Supplementary Material.

The probabilistic, data-assimilation approach presented here to reconstruct the LIS margins provides a new approach to reconstructing ice sheet margins and can be leveraged in several ways to further investigate the drivers of ice sheet collapse. As new data become available, they can be easily integrated to update posterior estimates, providing the scientific community with the basis for a constantly updating LIS reconstruction. The ALIS posterior 95% CI map can guide future data collection efforts by identifying regions of greatest uncertainty. The predictive power of ALIS also provides a method to determine deglaciation age and uncertainty for mapped geomorphic features (e.g., moraines, eskers, flow sets, etc.) for which ages are not always available. The spatially

continuous posterior with quantified uncertainties makes it convenient for assessing physics-based ice sheet models that similarly produce continuous fields. Also, while we have made conservative choices about data uncertainty and limiting constraints consistent with previous work (*9*), ALIS provides a new flexible framework for researchers familiar with these datasets to test alternative interpretations of geologic constraints; for example, in cases where limiting data are more closely tied to an ice margin or where different data types disagree (*57*). Finally, the method can be applied to other formerly glaciated regions to further understand the relationship between mechanical and climatic controls on deglaciation.

3.2 LIS deglaciation and Climate

To understand the relative importance of climatic and mechanical controls on the spatiotemporal patterns of LIS deglaciation, we first compare the ALIS reconstruction with a range of paleoclimate reconstructions at continental and regional scale (Fig. 3A-D, 4). Large changes in global mean surface temperature (GMST), Northern Hemisphere insolation, atmospheric CO_2, and ocean circulation throughout the deglaciation are expected to have significantly impacted the LIS by modulating surface mass balance. Increasing 65°N summer insolation and surface temperatures would have raised the equilibrium line altitude, bringing more of the ice-sheet surface into the ablation zone (*58*). At the same time, changes in atmospheric circulation due to the orographic effect of the LIS likely increased snow and ice accumulation in the west while splitting the mid-Latitude westerlies and promoting cooling over the interior (*59*).

The ALIS reconstruction highlights complex phasing between climate and ice loss. On a continental scale, we find that RAL resembles the trends of rising Northern Hemisphere summer insolation (*60*), increasing CO_2 concentration (*61*), and increasing NH temperature (*62*) and GMST (*63*) (3A-E). Accelerated retreat rate to the first maximum corresponds with rising GMST at ~17 ka, and the second maximum retreat rate aligns with maximum summer insolation at 65°N and warming temperatures during the early Holocene. In detail and at the regional scale, however, ice loss is at times out of phase with climate forcings. Early retreat from the LGME in the Atlantic sector precedes rising Northern Hemisphere insolation and GMST. As deglaciation continues, ice loss in the Keewatin sector most closely resembles warming and cooling patterns through the BA

and YD; however, maximum retreat in the Atlantic region precedes the BA, and retreat in the Hudson Bay region stays relatively constant through the entirety of the YD. Latitudinal trends in deglaciation are also ambiguous; for example, retreat from the terrestrial southern margin at similar latitudes (38-45N) spans nearly 7 kyr, and during the latter stages of deglaciation, the collapse of the northern Keewatin dome precedes the southern Labrador ice dome (Fig. 2).

A possible explanation for the regional decoupling of climate and ice sheet change may be that variability in regional climate across the LIS is not captured in high latitude ice cores and sea-surface temperature reconstructions. Modulations of the jet stream and ocean circulation, as well as orographic effects associated with ice-sheet topography, likely influenced local temperature and precipitation (*59, 64–66*). However, while these circulation changes may affect the spatial variability of surface mass balance, the largest swings in temperature over the deglaciation are still expected to be associated with millennial-scale climatic variability (BA, YD) that should influence the entire LIS. Yet as noted above, regional variability suggests additional mechanisms or forcings influencing retreat rates. (*4, 63, 67*).

Previous studies have hypothesized that an apparent decoupling between the LIS and climate results from the ice sheet being in positive mass balance across much of its surface during the early and middle deglaciation (*10, 58*). If the ablation zone were restricted to only the low-lying margins of the LIS, even moderate changes to the equilibrium line altitude—due to warming during the BA, for example—may have been insufficient to drive widespread surface melt and margin retreat. This would explain unresponsiveness of ice margins to millennial-scale temperature variations in some regions during deglaciation, and it would follow that other processes exerted a major control over spatiotemporal patterns of deglaciation.

3.3 Sediment, Ice Streams and Instability

The ALIS reconstruction highlights a critical link between retreat rates, ice streaming, and basal sediment conditions that offers a mechanism to explain the regional decoupling between climate and ice sheet retreat. In this mechanistic view, background climate forcing promotes LIS deglaciation at the continental and multi-millennial scale. Regionally, however, the spatial and temporal patterns of deglaciation are modulated by the distribution of soft, deformable sediment that facilitates ice

streaming and can trigger a mechanical instability that enhances retreat even in the absence of abrupt climate warming. These dynamic changes are amplified through the growth of proglacial lakes, whose calving promotes ice streaming and mass loss (*12, 25, 68*). This is in contrast to the prevailing view that rapid deglaciation, even on a regional scale, was primarily triggered by millennial-scale climate variability (*3, 4, 69–71*). Instead, we suggest that regional coincidences of ice sheet behavior and Northern Hemisphere climate—e.g. retreat during warming, advance during cooling—should be interpreted with caution and within a broader geologic context.

The proposed link between ice streaming and retreat identified here is supported by physics-based modeling that demonstrates the influence of subglacial geology on ice-sheet stability. In simulations of a Laurentide-like ice sheet, (*22*) found that identical shifts in climate forcing produced a much stronger response when fully developed ice streams were present than when they were absent, in some cases leading alternatively to rapid deglaciation or continued ice-sheet growth. Ice streaming in their model is a direct result of soft deformable till which increases sliding velocity and leads to positive feedback where sliding-induced frictional heating and melt water production at the bed further promotes ice velocity and discharge. While these simulations focus primarily on calving ice streams, they also show that significant mass loss occurs through surface melt in the ablation zone near the ice sheet terminus. This thinning-induced surface ablation offers a mechanism whereby continental LIS ice streams, many of which terminated on land in large lobes, could have promoted deglaciation even in the absence of proglacial lake or marine calving.

Previous authors have proposed a connection between subglacial bed conditions and ice sheet behavior during the deglaciation (*13, 14, 72*). (*72*) argued that most observed episodic retreat, re-advance and flow reorganization reflect dynamic readjustments of the ice sheet to changes in calving rates, bed conditions, or ice surface slope, while some other regional moraine systems reflect climatic forcings. Our findings are consistent with their hypothesis, however the details of their ice margin chronology and inferred retreat rates differ significantly from the ALIS—for example in the Canadian Interior Plains—due to the significant amount of data that has since become available [e.g. (*70, 73*)]. (*13, 14*) argued that retreat rates slowed specifically at the transition from soft-bedded continental sediments to the crystalline, hard-bedded Canadian Shield. Our results provide strong evidence supporting the hypothesis and, critically, demonstrate that subglacial geology exerts a dominant control in many other regions; for example, rapid retreat south of Hudson Bay coincides

with thick surficial deposits and the activation of ice streams, which was likely further amplified by the presence of proglacial Lake Agassiz-Ojibway (*56*).

In addition, through our analysis we explicitly identify deglacial ice streaming as the mechanism linking soft beds to faster deglaciation. The notable exception is for marine-terminating LGM streams, which occur early in the termination and without synchronous rapid retreat; for example, along the Atlantic coastline of eastern Canada and the US (Fig. 4E,F). We hypothesize that these regions represent a different ice streaming regime: rather than driving deglaciation, they may reflect millennial- to centennial-scale variability within a near-steady-state LIS. Indeed, records of iceberg rafted debris in the North Atlantic document that the largest of these features—the Hudson Strait ice stream—exported ice during Heinrich events (*74, 75*). The imprints of paleo ice streams along the continental shelf may be related to similar dynamics rather than to the rapid retreat at the onset of LIS deglaciation. It is also important to consider that these regions have scarce chronological constraints and thus short periods of rapid retreat—possibly analogous to that observed for the Fennoscandian Ice Sheet on the Norwegian continental shelf (*76*)—cannot be resolved. Still, our finding that ice streaming was regionally variable through time shows that rather than simply scaling with the size of the ice sheet, ice streams likely developed as a result of subglacial bed properties (and, in some cases, the presence of pro-glacial lakes) and consequently facilitated rapid deglaciation.

3.4 Implications for the role of ice streams in future deglaciation

Our results have implications for the future stability of modern ice sheets. Based on an argument that ice streaming activity scales with ice volume, (*15*) concluded that ice streams draining the Greenland and Antarctic ice sheets may switch off if those ice sheets continue to shed mass. Although at continental-scale the ALIS results appear to support that view, our regional analysis demonstrates that changes in ice stream activity are non-linear through time and are more closely linked to the availability of soft sediment than the overall ice sheet volume. It follows that as anthropogenic warming continues and ice sheets shrink over the 21st century and beyond, the patterns of retreat may be strongly dictated by ice streams, and in turn by the distribution of deformable basal sediment. Although the Greenland Ice Sheet currently has few land-terminating

ice streams, they may become more prevalent as its margins retreat inland. Assessing the future stability of the Greenland Ice Sheet will therefore require better characterization of subglacial geology than currently exists (*77–80*)

4 Materials and Methods

Geochronological and geomorphologic constraints

We use data from the recently published deglacial geochronological dataset of (*9*), hereafter NADD (North American deglacial dataset), which was used to construct the time-slice LIS reconstruction, NADI-1. NADD data are the result of screening and standardizing by (*9*) to allow for consistent interpretation of the data on a continental scale. We maintain that consistency and defer to the original authors' interpretations, calibrations, or classifications, except in specific cases described below. We consider two types of geochronological constraints from NADD: calibrated radiocarbon ages and ^{10}Be TCN ages (Fig. 1). Given the importance of TCN ages in dating paleo-margins, we updated the NADD with TCN data published since its release (*37–43*) (see appendix 4). The treatment of new TCN data and age calculation follows the exact methodology outlined in (*9*) to maintain consistency across the dataset. The updated NADD is available in the Supplemental Material. For this study, we focus primarily on the LIS and exclude ages associated with the Cordilleran Ice sheet (CIS); however, we include a subset of data to the west of the CIS-LIS saddle to capture the unzipping of the ice-free corridor (Fig. 1).

For the radiocarbon ages, we adopt the calibrated mean age and uncertainty from NADD and remove ages deemed 'unreliable' (quality level 3). (*9*) classified radiocarbon ages into three categories: 'ice-free', 'deglacial', and 'advance'. 'Ice-free' ages are minimum constraints on deglaciation and indicate only that the margin position was inward of the datum location at that time. 'Deglacial' ages are described in NADD as 'very closely' dating landscape emergence from under the former ice sheet, 'ideally within 100's of years'. 'Advance' ages constrain the timing of advance over a region and are thus maximum limiting ages on final deglaciation. These classifications inform the use of the data as limiting constraints on deglaciation (see section 4). For 'advance' ages, however, we only include those that represent the build-up to the local LGME in the Great Lakes region of

the southern LIS, which provides maximum ages for the LGME margin. Other 'advance' ages are removed since our model can only capture margins moving in one direction through time and thus cannot reproduce regional readvances.

For the TCN ages, we follow the methodology of (*9*), who took a conservative approach to define age uncertainty by combining the spread in measured ages of a given feature (moraine, boulder, etc.) with the internal and external uncertainty of the ^{10}Be measurements to determine 'minimum' and 'maximum' ages for each dated feature. Specifically, the 'mean age' is the mean of the individual sample ages, and for the minimum and maximum 1σ uncertainty, we take the oldest (youngest) age for the feature and then add (subtract) the average combined internal and external uncertainty from all ages used to date the feature. Following (*9*), outliers are removed before calculating the mean and uncertainty and features with fewer than two measured ages are excluded. This results in non-uniform uncertainties around a mean that we model as asymmetric normal distributions (see below). Additionally, we include synthetic limiting data to represent the six largest ice caps in the Canadian Arctic—the last remnants of the Innuitian Ice Sheet—and enforce that they must not deglaciate before the final demise of the LIS ($\sim$ 5 ka; see Appendix 4).

The moraine database of (*9*), while not exhaustive, contains the key features used in continental-scale mapping (Fig. 1, purple lines). We first filter the moraines for only those longer than 80 km, as the spatial length scale of our model is on the order of hundreds of km, so small features provide little additional information. Next, we take four equally spaced points along each moraine; for longer moraines, we add more points such that the spacing between points is at most 80 km. This ensures that all moraines provide information on the margin geometry while keeping the total number of data points relatively small. Where the moraine corresponds to a dated feature in the NADD TCN compilation, we assign the age and uncertainty to all points along the moraine and include them in the model as TCN ages. All sets of moraine points, whether dated or undated, are used to constrain the shape of the margin. We supplement the moraine data set with nine additional moraines from (*5, 70, 73, 81–85*) (see section 4).

Ice-stream geometries are from (*44*), who mapped all known features under the LIS. For each ice stream, we take the longest mapped longitudinal line (Fig. 1, red lines). Similar to the moraines, we reduce the dataset to only include lines longer than 200 km and then convert them into a set of equally spaced points (every 100 km; Fig. 1, red circles). In two locations, we extend the

mapped range of two ice streams to intersect with the local LGM extent—the James Lobe and the Lake Michigan Lobe—to ensure the lobes retreat northward continuously during deglaciation, as indicated by regional studies (*3, 64*).

Data Reduction

Bayesian statistical modeling of large datasets can have a high computational cost, mainly related to the inversion of large covariance matrices. For computational tractability, we take a few steps to reduce the dataset while retaining the most informative chronological constraints. First, we reduce the radiocarbon dataset, which is on the order of ~3000 data points in the NADD. We retain nearly all radiocarbon ages classified as 'deglacial,' which represent the best constraints on the location of the ice margin; we only discard data from this category when multiple ages are from the same site, in which case we take the oldest. The 'ice-free' radiocarbon ages are reduced based on their proximity to these 'deglacial' ages and the TCN ages, such that no radiocarbon age is within 80 km of another constraint; where ages overlap in space, we take the oldest—and therefore most constraining—age. The 'advance' ages are similarly reduced based on their proximity to each other. Young radiocarbon ages (< 16 ka) from the NADD that are beyond the well-documented ice limit east of Lake Michigan are removed from the dataset as they provide no additional constraints. We also reduce a small set of repetitive moraines on Melville Island to a simplified geometry similar to that used in the NADI-1 reconstruction (*9*). Two moraines related to a small ice free region in the US Midwest below the resolution of this model are removed (see section 4).

Ice Sheet Reconstruction Priors

The ice-sheet reconstruction ensemble represents a high-variance set of possible retreat scenarios (Fig. S2). The GIA-based reconstructions–ANU and ICE-7G (*32, 86*)–are included for their fit to global and local sea-level data as well as GPS and gravity observations. The ice-dynamic reconstructions are from a recent study (*87*), that provides a set of 27 reconstructions, which were constrained using deglacial chronologies and were originally described in (*33*). To ease computation, we reduce the 27-member ensemble to a smaller set of four representative ice chronologies using k-mean clustering. Finally, we include the overall 'preferred' reconstruction from (*87*)—NAIS-X—as

the seventh member of our ensemble. The final ensemble shows a range of predicted deglaciation age that is largest (up to 10 kyrs) near the LGM margin and is ~1-3 kyrs across the interior of the ice sheet (Fig. S2). While an even more diverse set of priors would be preferred, this ensemble still provides a range of scenarios for the assimilation. We also note that our statistical model is not limited by the priors and can deviate significantly from these predictions where required by the data.

Bayesian Modeling

We take a Bayesian approach to reconstruct a two-dimensional field of deglaciation time for the LIS. Rather than producing a single reconstruction, the model infers a distribution of possible deglaciation scenarios (the posterior) conditioned on the observations. The posterior is obtained by combining the likelihood function, which describes the data, with the hierarchical prior structure, which governs the deglaciation field, in this case, a Gaussian Process (GP). In this approach, uncertainty in our prior information (model parameters, ice sheet ensemble) as well as analytical uncertainty and sparsity in the geochronological data are propagated into the posterior. The following sections outline the structure of our statistical model and its implementation using the Python library PyMC (*88*). A schematic diagram of this approach is illustrated in S3.

Our model is hierarchical in that the joint posterior distribution of deglaciation time is based on conditional probabilities on four different levels:

$$p(f, \theta_l, \theta_p, \theta_o \mid y) \propto p(y \mid f, \theta_d)\, p(f \mid \theta_l, \theta_p, \theta_o)\, p(\theta_p, \theta_o)\, p(M \mid \theta_m) p(S \mid \theta_s) \tag{1}$$

The data level, $p(y \mid f, \theta_d)$, reflects our knowledge from the geochronological data. Specifically, it is the probability of the observed data, y, given the unknown, true deglaciation time, f, and the data-level hyperparameters θ_d, which relate to the uncertainty of the data (see section 4). The process level, $p\big(f \mid \theta_l, \theta_p\, \theta_o\big)$ models f as a GP and reflects our understanding of the spatial patterns of ice sheet margins (how smooth they are) and incorporates the prior information provided by the ice sheet ensemble (see section 4). Specifically, it is the probability distribution for f given the process-level hyperparameters θ_l (which describe the GP covariance), and the ice sheet model ensemble weights and global offset (θ_p and θ_o, respectively). The parameter level, $p(\theta_p, \theta_o)$, reflects our

initial predictions (probability distributions) of the hyperparameters. In the final model, the only hyperparameters with initial distributions are the ensemble weights and global offset (θ_p, θ_o, see section 4); all other hyperparameters are fixed values. However, we also run a regional calibration model where we consider the prior probability distributions on θ_l, or how smooth we imagine ice-sheet margins could be (see section 4); the optimized values for θ_l that this calibration yields are used for the continent-scale model. Finally, we add two soft constraints to the model that relate to the mapped moraines, $p(M \mid \theta_m)$, and the ice streams, $p(S \mid \theta_s)$, where M and S are the sets of features and θ_m θ_s represent the hyperparameters that define the penalty functions. These reflect additional knowledge based on assumptions about these geomorphic features and influence the posterior by adding penalties to the likelihood function (see section 4).

Data Level

The data level captures how the measured ages from NADD relate to the 'true' ice margin position, f. Since the geochronological constraints have asymmetric uncertainties, we represent each measured age, y_i, using a split-normal distribution with high and low one-sigma uncertainties, $\sigma_{H,i}$ and $\sigma_{L,i}$. The split-normal maintains Gaussian shape in both directions and integrates to 1, similar to a normal distribution (see 4).

We select $\sigma_{H,i}$ and $\sigma_{L,i}$ based on how a given constraint relates to f. TCN ages are assumed to directly reflect the ice margin position, so their mean age is taken to represent f at a given location and their minimum and maximum uncertainties are assigned to $\sigma_{L,i}$ and $\sigma_{H,i}$, respectively. The radiocarbon ages in general do not reflect f directly, so we expand their uncertainties such that the distribution acts as a limiting constraint in one direction. For ages indicating the absence of ice we start by assigning $\sigma_{H,i}$ and $\sigma_{L,i}$ the analytical uncertainties according to NADD (see 4), then we increase the higher (older) uncertainty, $\sigma_{H,i}$, to reflect the wide range of ages over which the margin could have retreated before deposition of the dated sample. For the 'ice-free' data, we increase $\sigma_{H,i}$ by an arbitrarily large number (7.5-kyr) such that it offers effectively no constraint in one direction. For the 'deglacial' data, which make up 17% of all minimum-limiting ages, the uncertainty is increased by 2-kyr based on the proposition by (*9*) that these ages were likely 'near the margin within 100s of years of their deposition'. The choice of 2-kyr allows for the possibility of a longer lag time than the '100' years proposed by the original authors. For the 'advance' age,

the limiting constraint is flipped, so we apply the analytical uncertainty to $\sigma_{H,i}$, and add 3 kyr to the lower uncertainty bound to reflect the possible lag time between deposition of the dated unit and the subsequent deglaciation in that region. The choice of 3 kyr is based on regional studies that suggest the vast majority of advance ages have less than a 3-kyr lag before subsequent retreat (*3, 64*). Finally for all the constraints, we add a small adaptive white noise component to the data uncertainty, which helps with the sampling algorithm (*89*). The effective uncertainty for each observation is taken as the square root of the sum of squares of the reported dating uncertainty and a white noise amplitude (σ_{wn}), which is learned from the regional calibration model described below (4).

To define the data level in our model, we take the joint log-likelihood of all observations:

$$\log p(y \mid f, \theta_d) = \sum_i \log p\left(y_i \mid f_i, \theta_{d,i}\right). \tag{2}$$

where $p\left(y_i \mid f_i, \theta_{d,i}\right)$ is a split-normal distribution for a given data point and $\theta_{d,i}$ represents both $\sigma_{H,i}$ and $\sigma_{L,i}$ which define the shape of the distribution.

Process Level

The process level captures the inherent spatial and temporal variability of ice-sheet retreat. We take a common approach in the data assimilation literature by defining the field of interest as a Gaussian Process (*20, 36, 89, 90*). Specifically, we define the true deglaciation time as a latent Gaussian process:

$$p\left(f \mid \theta_p, \theta_o, \theta_l\right) = N\left(f \,\middle|\, m(\theta_p, \theta_o),\ C(\theta_l)\right), \tag{3}$$

where $m(\theta_p)$ is the prior mean and $C(\theta_l)$ is the covariance matrix, or kernel, determined by the process-level hyperparameters θ_l. The mean is the weighted linear combination of the ice-sheet model ensemble plus a global offset; the weights, θ_p, and offset, θ_o, are given prior distributions (see 4) and are inferred jointly with f through posterior sampling, allowing the model to adapt the weights according to the geologic constraints.

The kernel, $C(\theta_l)$, describes how data points in space and time relate to one another and is an essential element of our model. It determines the spatial complexity or smoothness of ice margin retreat. Intuitively, one can think of it as describing how informative a single data point is about a

given region. In many geoscience applications, 2D spatial data are modeled with 'isotropic' kernels that assume covariance is the same in all directions (*36, 89*). However, visual inspection of the geochronological constraints shows this is a bad assumption: ages tend to vary more smoothly along the margin than across it, particularly in regions where the rate of retreat is slower. In other words, the rate of retreat from one margin to the next has a different variance than undulations along the margin itself. This is essentially a product of how we are modeling a time field using only spatial dimensions.

To address this issue, we develop a kernel matrix based on two principles: covariance between locations decreases 1) with spatial distance and 2) with time of deglaciation. These effects are captured by individual radial basis functions (RBF) that are multiplied together to generate a kernel such that two points must be close in both space and time to have a high covariance. The first RBF determines covariance using the spatial (great circle) distance between locations scaled by a characteristic spatial length scale hyperparameter, θ_{ls} (*91*). For the second RBF, we follow previous literature that defines covariance based on the behavior of a model prior or ensemble of priors (*36*). Here, we use the NAIS-X (preferred) reconstruction from (*87*) to define the 'temporal' distance between two points by sampling the model at each location and taking the difference in the predicted deglaciation times. The temporal RBF has an associated 'temporal' length scale hyperparameter, θ_{lt}, that controls the strength of covariance with temporal distance. The combined kernel matrix is:

$$k_{\text{joint}}(i,j) = \theta_\sigma^2 \exp\left(-\frac{1}{2}\left[\frac{\|\mathbf{x}_i - \mathbf{x}_j\|^2}{\theta_{ls}^2} + \frac{(T_i - T_j)^2}{\theta_{lt}^2}\right]\right)$$

where θ_σ is the kernel variance. In total, the covariance hyperparameters, θ_l, include θ_{ls}, θ_{lt}, and θ_σ, which are assigned values based on a regional experiment described below.

We conduct a sensitivity analysis to understand the bias introduced by employing a single prior model to define the temporal component of the covariance matrix. We run the model with temporal covariance defined by two different ice sheet reconstructions from (*87*): the NAIS-X (preferred) reconstruction and reconstruction '9852'. The GP mean is held constant in the test to isolate the effect of the temporal variance. We find that the influence of reconstruction choice has a relatively small impact on the posterior (generally less than < 0.5 kyr; Fig. S4). Larger differences (1-3 kyr) occur in some places near the LGME margins and in the high Arctic near modern ice caps, likely due to differences in how these reconstructions capture the exact location of the LGM margin and

late Holocene ice dynamics.

Moraines and Ice Stream Constraints

Ice streams are incorporated as 'soft constraints' to ensure deglaciation does not happen 'backwards' or downstream along mapped ice flow. In practice, the constraint eliminates erroneous deglaciation patterns and refines the location of ice domes in data-poor regions like the Keewatin Sector. For each ice stream, we take the ordered set of points along flow and arrange them into adjacent pairs. During sampling, the difference in predicted age at the point pairs—upstream minus downstream—is calculated and then compared to a penalty function. The penalty function is a 'soft hinge' function, which returns a penalty near zero where the difference is negative (correct sequence) and an increasingly greater penalty the more positive the difference is (see 4 for a full description of the function).

Moraines are implemented as soft constraints on 1) the direction of deglacial retreat and 2) the geometry of the ice margin. For each feature, we take pairs of points along the moraine, and for each pair we find a third point offset (10 km) perpendicular to the ridge on the upstream side as interpreted by (*9*). The directional constraint enforces that the upstream side is younger than the moraine ridge, using the same soft hinge penalty as the ice stream constraint, applied to the difference between the offset point age and the average age of the two on-moraine points. The geometric constraint penalizes configurations where the contour runs across the moraine rather than along it. This is achieved by computing the ratio of the squared on-moraine pair age difference to the total squared age variation across both directions. When the along-moraine difference dominates, this ratio approaches one and incurs a large penalty, but when the cross-moraine difference dominates, the ratio approaches zero and the penalty is negligible. Both penalties are summed over all triplets to form a log-potential contribution to the model. The total penalty is also multiped by a factor of four, which was found to substantially increase the posterior fit to the moraines, while only decreasing the fit to the geochronological constraints by less then 1%.

Parameter Level

The parameter level captures the prior distributions, or our 'prior knowledge', of all the hyperparameters. Some hyperparameters are modeled empirically, i.e., assigned fixed values. These are the

data uncertainties, θ_d, and the soft constraint parameters, θ_d and θ_s, used to construct the penalty functions for the moraines and ice streams.

A Dirichlet distribution with a concentration parameter of 0.5 is used to describe the prior weights for the ice sheet models, θ_p, that determine the GP mean. Conceptually, this reflects a prior belief that one or a few models should be better suited to match the data rather than an even blend across the ensemble. A global offset parameter, θ_o, is added to the linear combination to account for systematic biases in the ice sheet priors. θ_o is given a prior Normal distribution centered at zero with a standard deviation of 0.5 in normalized time units.

Finally, we conduct a two-stage approach to identify the covariance length scale hyperparameters θ_σ,θ_{ls}, θ_{lt}, σ_{wn}. We seek to identify parameters that capture the data to the fullest extent without introducing high spatial variability that is beyond the scope of the available constraints. In other words, we seek the smoothest interpolation of data that still fits the available constraints. This could be accomplished with a fully Bayesian approach in which these hyperparameters are 'learned' during sampling. However, this is computationally prohibitive given the size of the dataset. Instead, we identify a representative subregion–from southern New York up to the Labrador Sector of the LIS–that includes both data dense and sparse areas to allow the model to learn an appropriate length scale (Fig. S6). Log-normal prior distributions are used to describe the covariance matrix hyperparameters. This helps ensure the parameters remain positive during sampling. For the mean of the distribution, we chose reasonable values given the pattern of the data: θ_{ls}, θ_{lt}, and θ_σ are assigned means of 350 kyr, 2.0 kyr, and 1.0 (unitless), respectively. We select 0.4 in log-space as the sigma on these distributions to generate the weakly informative priors. Finally, a half Normal prior distribution is placed on the white noise component, σ_{wn}, with a standard deviation of 0.02 kyr. The half normal was chosen to encourage a high prior density near zero (no white noise).

Sampling and prediction for the regional model follow the methods described for the whole ice sheet model in section 4 below. The regional model predictions accurately replicate the geochronological data and produce realistic deglacial margins (Fig. S6). We take the greatest density (mode) from the posterior estimates of the four learned variables: θ_{ls}, 664; θ_{lt}, 3.0; θ_σ, 0.31; and σ_{wn}, 0.001 S6). A consequence of this methodology is that the posterior of our full model may underrepresent uncertainties related to the uncertain length scale. However, comparing the uncertainty in the regional-fully Bayesian (Fig. 2) subset with the continental empirical Bayesian run (Fig. S6,

right panel), we find similar values.

Posterior Sampling and Prediction

The model performs Bayesian inference using a No-U-Turn Sampler (NUTS) implemented in the Blackjax library within PyMC. NUTS draws samples from the joint posterior distribution of the latent deglaciation field, f, and model hyperparameters, θ, conditioned on the constraints described above. Before sampling, the time domain is normalized. Four sampling chains with 2000 samples each were run to ensure all chains converged on the same posterior distribution. Each chain was initiated with 4000 'tuning' draws that are not included in the posterior. The chains were assessed to ensure they are well-conditioned: no divergences occur and all parameters result in a Gelman–Rubin statistic of less than 1.1 (*89*). Sampling for the regional model is the same as the full model except for the inclusion of the four 'learned' hyperparameters.

We assess the fit of the posterior at each data location by comparing the median prediction and 95% CI to the observed age and uncertainty. The model fits 93.9% of the limiting data and 77.0% of the TCN ages within data uncertainty (Fig. S5). The few places where the model is unable to fit the TCN ages are regions with high spatial complexity (smaller length scales than our continental-scale model can capture), or conflicting radiocarbon and/or TCN ages. In general, where the model cannot fit both data types, it prefers to fit the limiting data where possible since the uncertainties in radiocarbon dating are much smaller; i.e., misfits to radiocarbon ages can result in greater penalties in the likelihood function.

We also assess the posterior weights for the ensemble of ice sheet reconstructions used as priors in the Bayesian model. The posterior distribution of these weights reveals a preference for one of the prior ensemble reconstructions—a climate-forced and ice-physics-based reconstruction from (*87*) (reconstruction #9852) originally described in (*33*). The preferred ensemble member has a posterior mean weight of 52% (34-68% 95% CI), while the second preferred member has a weight of only 19% (8-29% 95% CI). The Bayesian model then updates the weighted prior by up to 3 kyr in certain locations to produce the ALIS posterior, demonstrating that the model is learning additional information from the data (Fig. S11).

We make out-of-sample predictions for deglaciation time across North America on a lat-lon grid (resolution $\sim$ 30 km) by calculating the posterior predictive distribution for those locations

with the PyMC function 'sample_posterior_predictive', which works by conditioning a set of new predictions using the posterior draw for the latent field, f. In theory, any grid resolution is possible; $\sim$ 30 km was chosen to be well below the spatial complexity of the field—i.e. linear interpolation at higher resolution will not skew the results. The function provides predictions based on each sample, or draw, from the posterior, which includes all uncertainty related to data uncertainty itself, the conditional uncertainty of the GP kernel, and the posterior distributions of the hyperparameters and ice sheet models (prior mean function). From this distribution of predictions, we calculate the median deglaciation time as well as the 5%, 16%, 84% and 95% CI (Fig. 2). Posterior predictions are masked using the LGME from (*9*). Similar to the grid, we also calculate the posterior distribution on points sampled directly from the mapped LMGE from (*9*) (Fig. 2). To derive retreat rates, we calculate the magnitude of the gradient (kyr/km) for every predicted grid, invert it to get km/kyr, and then calculate the mean and percentiles from all the draws (Fig. S8). Selected time slices of the posterior are plotted individually and compared to a previous LIS reconstruction in Fig. S7.

We calculate the posterior distribution at specific locations to provide age estimates for key events in the deglaciation of the LIS discussed in section 2.1. We predict ages for points along the suture zone, mapped approximately from (*9*), following the same approach for out-of-sample predictions on a grid (section 4; Fig. S9). The age estimate for the Hudson Bay saddle collapse was found by treating the posterior deglaciation age field as a 3D space where age is the vertical dimension and taking the col (lowest point, oldest age) of the saddle connecting the Keewatin and Labrador domes (age minima). Finally, the age of disappearance for the domes is taken as the median and 95% CI for the oldest age in each region.

Model Validation

While the model provides good fits to the data within uncertainty (4, Fig. S10), we still need to validate its predictive capabilities across the entire continent. We follow a common approach in data assimilation and Bayesian inference literature in which we attempt to recreate a simulated field using synthetic data drawn from that field (*36, 92*). This allows us to assess whether the data density, data uncertainties, and model parameters are well-posed to actually determine the pattern of deglaciation across North America.

We use an ice sheet reconstruction of deglaciation from (*87*) that was not used in our prior

ensemble to represent the 'true' field (reconstruction #1263). Synthetic ages are sampled from that field at the real locations of our data constraints. The synthetic ages and real uncertainties are then used in the model as described in previous sections to infer a posterior estimate for deglaciation. The posterior is finally used to predict the mean deglaciation age on a grid. For this synthetic test, we leave out the ice stream and moraine constraints as they don't exactly match the 'known' field we invert for; however, their inclusion in our final model should only serve to further improve the posterior.

The posterior fits 99.6% of synthetic TCN ages and 100% of the radiocarbon limiting ages. The difference between the posterior and the 'true' reconstruction is near zero where TCN data is available and is less than 2 kyr across most regions with only limiting ages (Fig. S10). In most cases where there is bias, it is towards older ages as most of the radiocarbon is minimum limiting. The geometry of the margins in the posterior where there is bias largely resembles the GP weighted mean (the linear combination of ice-sheet ensemble members) that is inferred during sampling. This is an intentional product of the data assimilation approach: where data is missing, we defer to our prior knowledge, in this case, the weighted mean of the ice sheet reconstructions.

The regions of bias also correlate with high uncertainty in the posterior (Fig. S10E). The magnitude of the high-end uncertainty of the posterior (95th percentile minus median) is comparable to or greater than the bias towards older ages, which suggests that although there is some bias, it is captured within uncertainty—another intended feature of the data assimilation approach (Fig. S10D,F). This test thus gives us confidence that the model is capable of inferring the 'true' pattern of deglaciation and that, where data are limiting or sparse, the model is acknowledging realistic uncertainty and defaulting to the 'best-guess' from the ice sheet model priors.

Posterior Analysis and Statistics

We compare the ALIS reconstruction to maps of sediment distribution and type across North America. These include maps of average soil and sedimentary deposit thickness from (*55*), as well as average grain size, sediment distribution, and bedrock geology from (*54*). While, the sediment thickness map of (*55*) likely includes post-glacial deposits, the key regions of thick deposits are in good agreement with field evidence for Quaternary sediments that pre-date the last glacial period (*72, 93*) (Fig. S6; see section 4). For example, the thick deposits in the Hudson Bay

Lowlands comprise tills and inter-till marine and lacustrine deposits from previous glaciations and inter-glacials (*94, 95*). Additionally, the map from (*55*) is consistent with the mapping of continuous sediment cover from (*54*) (Fig. S8).

We first linearly interpolate each dataset onto the same grid as the ALIS posterior. To derive a time series for change in each proxy over time, grid cells are binned and averaged based on the deglaciation age predicted by the posterior. This process was repeated for every draw of the posterior and the individual time series stacked and averaged to derive CI (Fig. 3). Cells that have no information—generally modern oceans, lakes and the remote regions of the Canadian archipelago—are excluded.

To calculate the proportion of the active margin that is lake-terminating, we use an updated model prediction for North American glacial lakes (*25*). The model was run the same as in (*25*) but with the updated margin chronology from (*9*). Time series are then derived following the same protocol as for other proxies described above.

We also use the posterior to derive ages for the mapped ice streams (*44*). While predicting exactly when ice streams were active is challenging as they are known to turn off and on over short time scales (*96*)–a problem of all paleo ice stream studies (*15*)–we can still determine times when they could have been active since the margin needs to be at or very close to the mapped stream (see 4). Specifically, the number of active ice streams at a given time is calculated, predicting the deglaciation time (and uncertainty) at the start and end of the mapped feature following the same protocol for predicting on a grid (4)

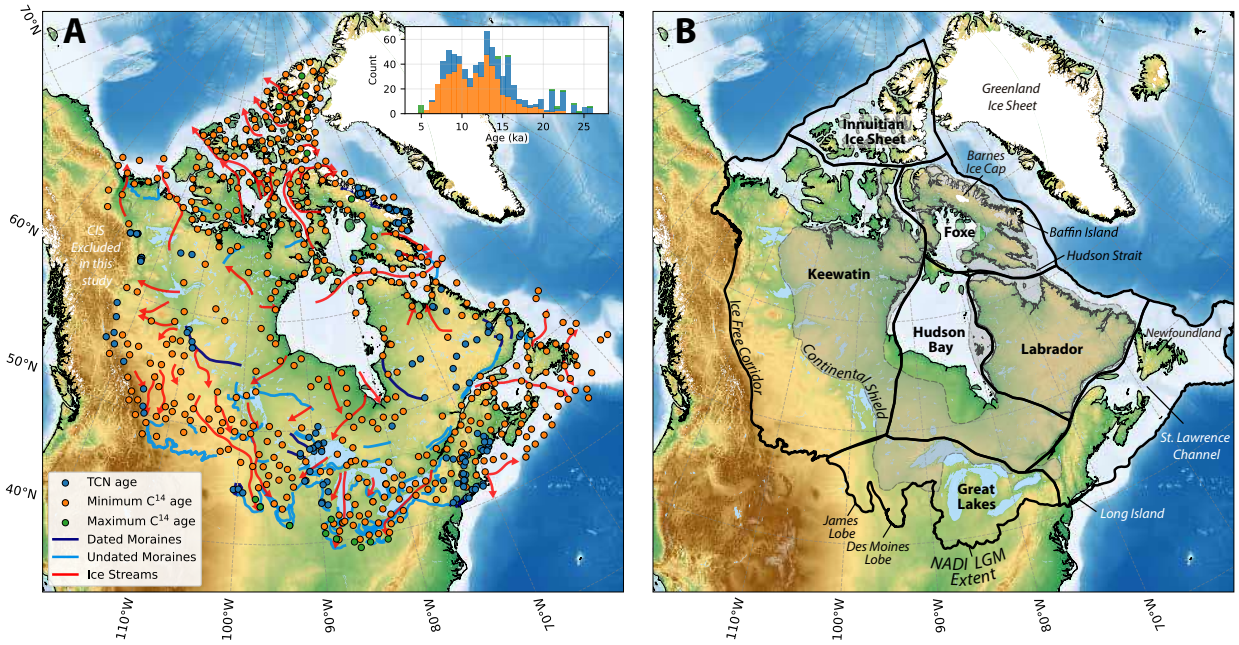


Figure 1: **Geochronological and geomorphic constraints used in the ALIS reconstruction.** In (**A**), TCN ages (blue circles) and minimum/maximum limiting radiocarbon (orange/green circles) are from (*9*), with additional data from (*37–43*); Red lines indicate ice streams from (*44*) and purple and light blue lines indicate dated or undated moraines from (*9*), respectively. Note that dated moraines are represented in the model by a series of points constraints (see 4). Inset histogram shows the age distribution (mean) of chronological constraints; data types in each bin are stacked. In (**B**), labeled regions are generalizations of the sectors discussed in (*9*). The outer black line is the maximum extent of the LIS (LGME) from the NADI-1 reconstruction (*9*). Grey shaded area shows the extent of the Canadian Shield.

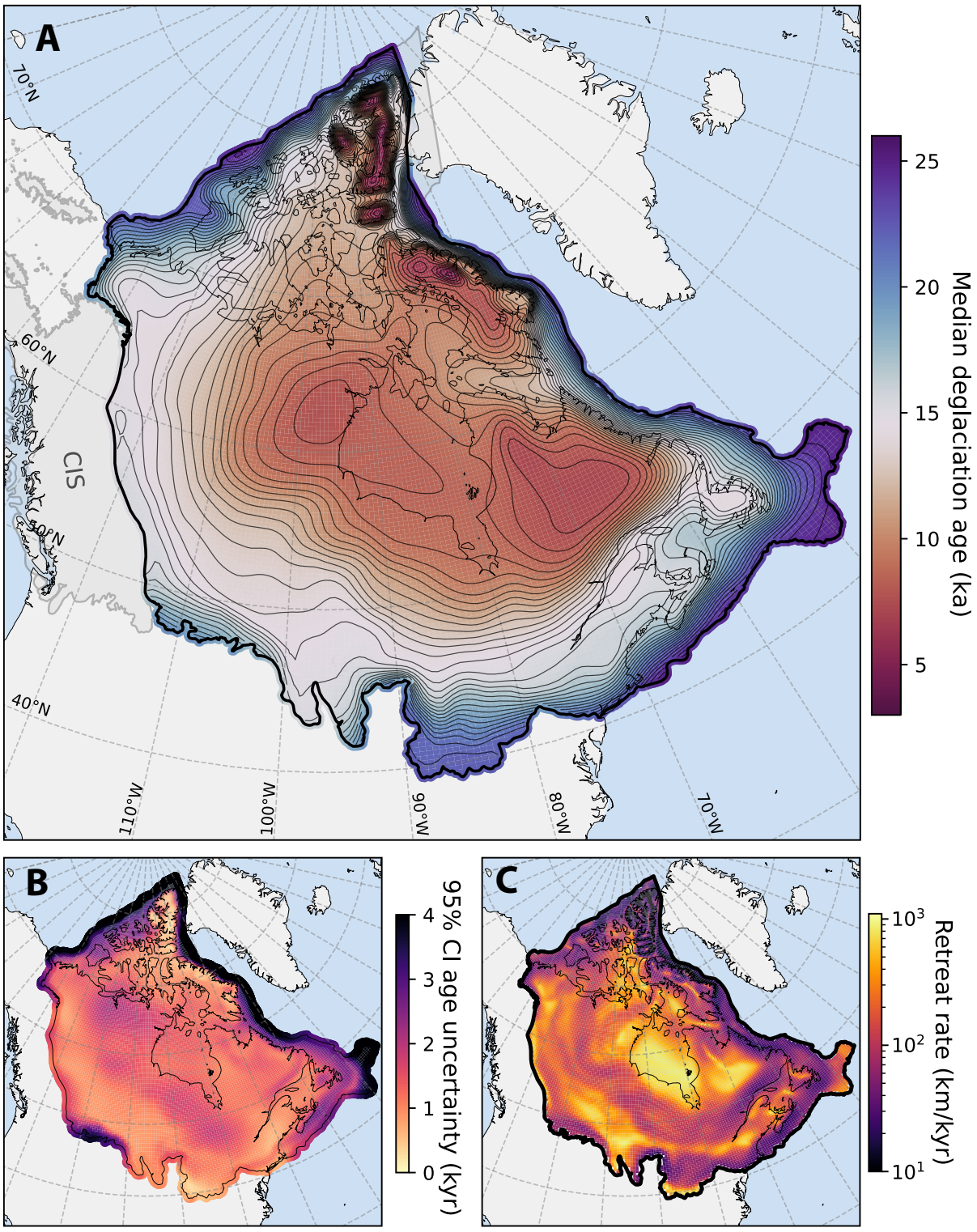


Figure 2: **The data Assimilation-based Laurentide Ice Sheet (ALIS) margin reconstruction of the last deglaciation and associated uncertainty.** (**A**) Posterior median estimate of deglaciation time and paleo margins (contours are 0.5 kyr intervals); (**B**) associated uncertainty (95% confidence intervals); (**c**) posterior median retreat rates (km/kyr). The thick black line in each panel shows the LGME from (*9*) with the Cordilleran Ice Sheet (CIS) in gray.

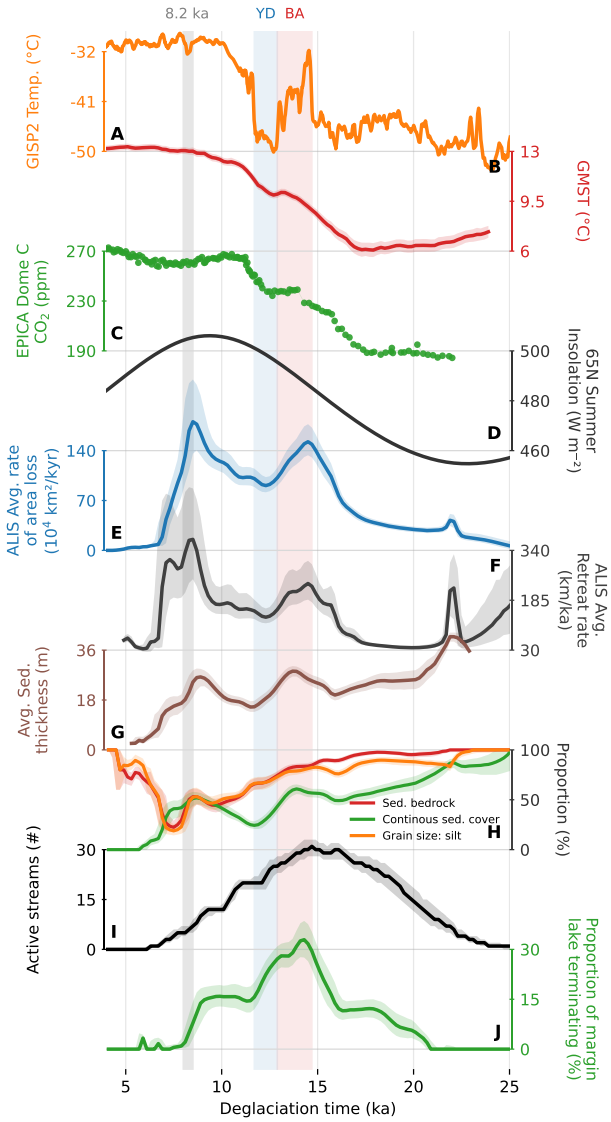


Figure 3: **Last Termination and the ALIS reconstruction on a continental-average scale.** Note, the ALIS reconstruction was used alone to generate panels (**E**-**F**) and in combination with other datasets to generate (**G**-**J**). (**A**) GISP2 Temperature reconstruction (*62*); (**B**) global mean surface temperature (*63*); (**C**) CO_2 concentration from the EPICA Dome C ice core (*61*); (**D**) 65°N July insolation (*60*); (**E**) average rate of ALIS area loss (RAL); (**F**) average ALIS retreat rate (RR); (**G**) average sediment thickness along retreating ALIS margin (*55*); (**H**) proportion of the margin that overlies sedimentary bedrock (red), regions with continuous sediment cover (green), and regions with average grain size of silt (orange) (*54*); (**I**) number of active ice streams (*44*); (**J**) proportion of margin that terminates in a lake (*25*). See section 4 for calculation of time series from gridded and geomorphic datasets (**G**-**J**). Shaded regions in (**E**-**J**) correspond to the 95% CI. Bølling–Allerød (BA), Younger Dryas (YD), and the 8.2 ka event are indicated with red, blue, and black bars.

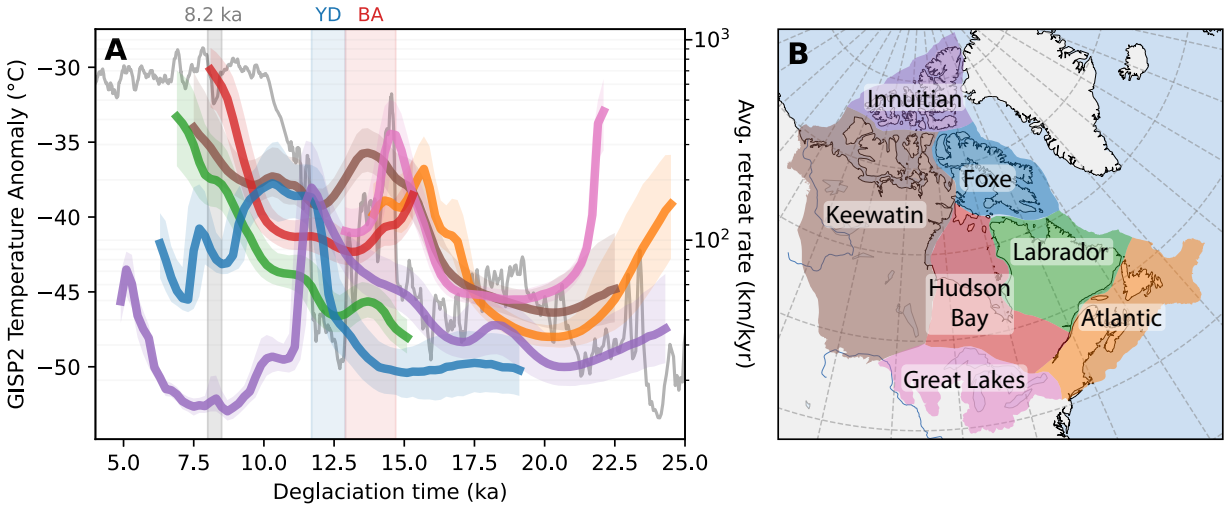


Figure 4: **Regional variability in the average retreat rate (RR) of the ALIS reconstruction.** (**A**) Timeseries of the average retreat rate corresponding to regions shown in (**B**). For reference, the GISP2 temperature reconstruction from (*62*) is shown in (**A**), as well as the Bølling–Allerød (BA; red), Younger Dryas (YD; blue), and the 8.2 ka event (black bar). Right vertical axis is in log scale.

Table 1: **Summary of model parameters used in the Bayesian framework.**

Parameter	Description
f	Latent deglaciation age field
y	Observed dating ages
θ_d	Observation uncertainty
θ_m	Moraine constraint hyperparameters
θ_s	Ice stream constraint hyperparameters
θ_{ls}	Spatial lengthscale
θ_{lt}	Temporal lengthscale
θ_σ	GP amplitude
σ_{wn}	White noise amplitude
θ_p	Prior mean blend weights
θ_o	Prior mean offset

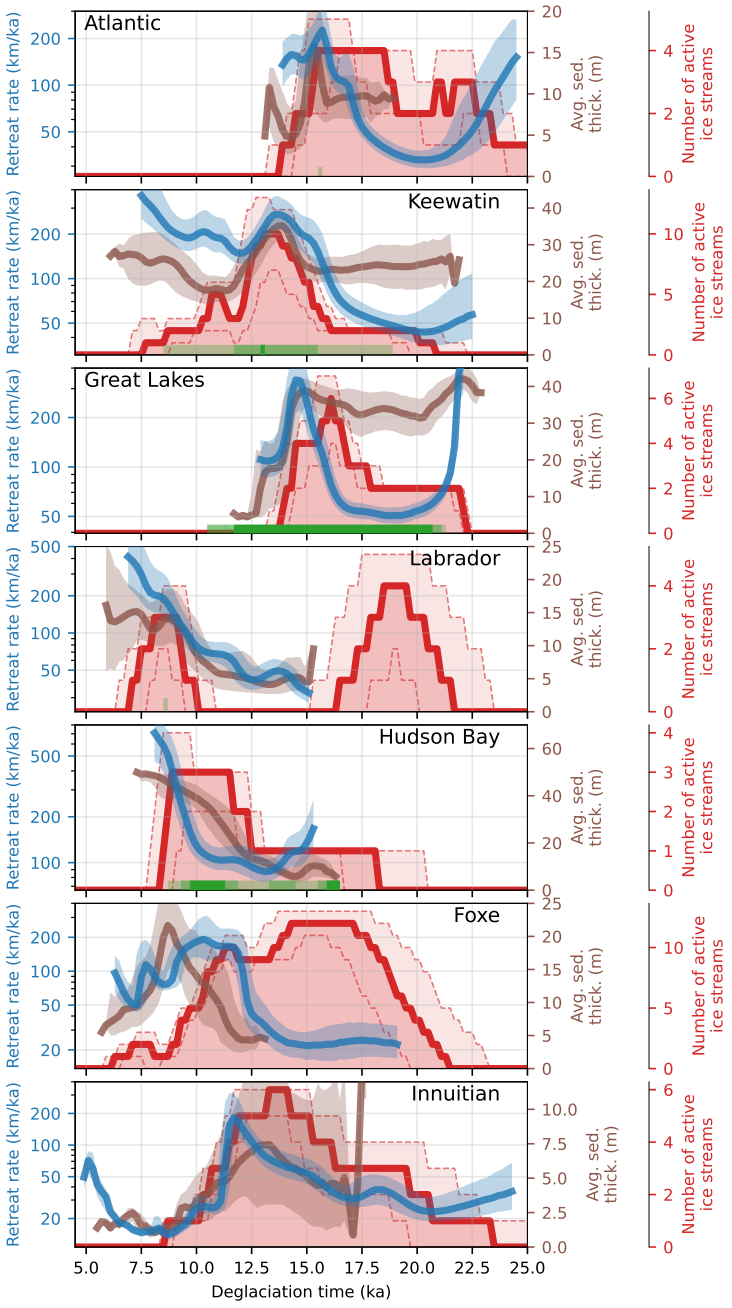


Figure 5: **Investigating controls on regionally variable deglaciation.** For each sector, the rate of area loss (blue) is compared to average sediment thickness along the active margin (brown) and the number of active ice streams (red). Note, sediment thickness time series are only plotted for periods where sediment thickness data is available (*55*). Retreat rate time series are shown in log scale. Dark, medium, and light green bars indicate times when 50%, 30%, and 10% of the active margin was lake terminating, respectively.

References and Notes

1. G. H. Denton, *et al.*, The Last Glacial Termination. *Science* **328** (5986), 1652–1656 (2010), doi:10.1126/science.1184119, https://www.science.org/doi/10.1126/science.1184119.

2. P. U. Clark, *et al.*, The Last Glacial Maximum. *Science* **325** (5941), 710–714 (2009), doi:10.1126/science.1172873, https://www.science.org/doi/10.1126/science.1172873.

3. S. L. Heath, T. V. Lowell, The Late Glacial Advance of the James Lobe, South Dakota, Suggests Climate-Driven Laurentide Ice Sheet Behavior. *Quaternary* **8** (4), 58 (2025), doi:10.3390/quat8040058, https://www.mdpi.com/2571-550X/8/4/58.

4. A. S. Dalton, M. Margold, H. E. Dulfer, S. L. Norris, L. Tarasov, Response of North American ice sheets to the Younger Dryas cold reversal (12.9 to 11.7 ka). *Earth-Science Reviews* **255**, 104845 (2024), doi:10.1016/j.earscirev.2024.104845, https://www.sciencedirect.com/science/article/pii/S0012825224001727.

5. N. E. Young, *et al.*, Pulsebeat of early Holocene glaciation in Baffin Bay from high-resolution beryllium-10 moraine chronologies. *Quaternary Science Reviews* **270**, 107179 (2021), doi:10.1016/j.quascirev.2021.107179, https://www.sciencedirect.com/science/article/pii/S0277379121003863.

6. A. D. Wickert, *et al.*, Marine-Calibrated Chronology of Southern Laurentide Ice Sheet Advance and Retreat: ˜2,000-Year Cycles Paced by Meltwater–Climate Feedback. *Geophysical Research Letters* **50** (10), e2022GL100391 (2023), _eprint: https://agupubs.onlinelibrary.wiley.com/doi/pdf/10.1029/2022GL100391, doi:10.1029/2022GL100391, https://onlinelibrary.wiley.com/doi/abs/10.1029/2022GL100391.

7. A. Breckenridge, *et al.*, A new glacial varve chronology along the southern Laurentide Ice Sheet that spans the Younger Dryas–Holocene boundary. *Geology* **49** (3), 283–288 (2020), doi:10.1130/G47995.1, https://doi.org/10.1130/G47995.1.

8. T. V. Lowell, *et al.*, Near-constant retreat rate of a terrestrial margin of the Laurentide Ice Sheet during the last deglaciation. *Geology* **49** (12), 1511–1515 (2021), doi:10.1130/G49081.1, https://doi.org/10.1130/G49081.1.

9. A. S. Dalton, *et al.*, Deglaciation of the north American ice sheet complex in calendar years based on a comprehensive database of chronological data: NADI-1. *Quaternary Science Reviews* **321**, 108345 (2023), doi:10.1016/j.quascirev.2023.108345, https://www.sciencedirect.com/science/article/pii/S0277379123003931.

10. D. J. Ullman, A. E. Carlson, F. S. Anslow, A. N. LeGrande, J. M. Licciardi, Laurentide ice-sheet instability during the last deglaciation. *Nature Geoscience* **8** (7), 534–537 (2015), doi:10.1038/ngeo2463, https://www.nature.com/articles/ngeo2463.

11. A. Abe-Ouchi, *et al.*, Insolation-driven 100,000-year glacial cycles and hysteresis of ice-sheet volume. *Nature* **500** (7461), 190–193 (2013), doi:10.1038/nature12374, https://www.nature.com/articles/nature12374.

12. M. C. M. Winsborrow, C. D. Clark, C. R. Stokes, What controls the location of ice streams? *Earth-Science Reviews* **103** (1), 45–59 (2010), doi:10.1016/j.earscirev.2010.07.003, https://www.sciencedirect.com/science/article/pii/S0012825210000838.

13. P. U. Clark, Unstable Behavior of the Laurentide Ice Sheet over Deforming Sediment and Its Implications for Climate Change. *Quaternary Research* **41** (1), 19–25 (1994), doi:10.1006/qres.1994.1002, https://www.sciencedirect.com/science/article/pii/S0033589484710027.

14. J. M. Licciardi, P. U. Clark, J. W. Jenson, D. R. Macayeal, DEGLACIATION OF A SOFT-BEDDED LAURENTIDE ICE SHEET. *Quaternary Science Reviews* **17** (4), 427–448 (1998), doi:10.1016/S0277-3791(97)00044-9, https://www.sciencedirect.com/science/article/pii/S0277379197000449.

15. C. R. Stokes, M. Margold, C. D. Clark, L. Tarasov, Ice stream activity scaled to ice sheet volume during Laurentide Ice Sheet deglaciation. *Nature* **530** (7590), 322–326 (2016), doi:10.1038/nature16947, https://www.nature.com/articles/nature16947.

16. R. B. Alley, D. D. Blankenship, C. R. Bentley, S. T. Rooney, Deformation of till beneath ice stream B, West Antarctica. *Nature* **322** (6074), 57–59 (1986), doi:10.1038/322057a0, https://www.nature.com/articles/322057a0.

17. L. K. Zoet, N. R. Iverson, A slip law for glaciers on deformable beds. *Science* **368** (6486), 76–78 (2020), doi:10.1126/science.aaz1183, https://www.science.org/doi/full/10.1126/science.aaz1183.

18. C. Stokes, C. Clark, Palaeo-ice streams. *Quaternary Science Reviews* **20** (13), 1437–1457 (2001), doi:10.1016/S0277-3791(01)00003-8, https://linkinghub.elsevier.com/retrieve/pii/S0277379101000038.

19. M. R. Bennett, Ice streams as the arteries of an ice sheet: their mechanics, stability and significance. *Earth-Science Reviews* **61** (3), 309–339 (2003), doi:10.1016/S0012-8252(02)00130-7, https://www.sciencedirect.com/science/article/pii/S0012825202001307.

20. C. D. Clark, *et al.*, Growth and retreat of the last British–Irish Ice Sheet, 31 000 to 15 000 years ago: the BRITICE-CHRONO reconstruction. *Boreas* **51** (4), 699–758 (2022), _eprint: https://onlinelibrary.wiley.com/doi/pdf/10.1111/bor.12594, doi:10.1111/bor.12594, https://onlinelibrary.wiley.com/doi/abs/10.1111/bor.12594.

21. H. D. Pritchard, R. J. Arthern, D. G. Vaughan, L. A. Edwards, Extensive dynamic thinning on the margins of the Greenland and Antarctic ice sheets. *Nature* **461** (7266), 971–975 (2009), doi:10.1038/nature08471, https://www.nature.com/articles/nature08471.

22. A. A. Robel, E. Tziperman, The role of ice stream dynamics in deglaciation. *Journal of Geophysical Research: Earth Surface* **121** (8), 1540–1554 (2016), _eprint: https://agupubs.onlinelibrary.wiley.com/doi/pdf/10.1002/2016JF003937, doi:10.1002/2016JF003937, https://onlinelibrary.wiley.com/doi/abs/10.1002/2016JF003937.

23. A. J. Payne, A. Vieli, A. P. Shepherd, D. J. Wingham, E. Rignot, Recent dramatic thinning of largest West Antarctic ice stream triggered by oceans. *Geophysical Research Letters* **31** (23) (2004), _eprint: https://agupubs.onlinelibrary.wiley.com/doi/pdf/10.1029/2004GL021284,

doi:10.1029/2004GL021284, https://onlinelibrary.wiley.com/doi/abs/10.1029/2004GL021284.

24. B. J. Stoker, *et al.*, The collapse of the Cordilleran–Laurentide ice saddle and early opening of the Mackenzie Valley, Northwest Territories, Canada, constrained by ^{10}Be exposure dating. *The Cryosphere* **16** (12), 4865–4886 (2022), doi:10.5194/tc-16-4865-2022, https://tc.copernicus.org/articles/16/4865/2022/.

25. J. Austermann, *et al.*, Glacial Isostatic Adjustment Shapes Proglacial Lakes Over Glacial Cycles. *Geophysical Research Letters* **49** (24), e2022GL101191 (2022), doi:10.1029/2022GL101191, https://agupubs.onlinelibrary.wiley.com/doi/10.1029/2022GL101191.

26. A. D. Wickert, R. S. Anderson, J. X. Mitrovica, S. Naylor, E. C. Carson, The Mississippi River records glacial-isostatic deformation of North America. *Science Advances* **5** (1), eaav2366 (2019), doi:10.1126/sciadv.aav2366, https://www.science.org/doi/10.1126/sciadv.aav2366.

27. A. S. Dalton, *et al.*, An updated radiocarbon-based ice margin chronology for the last deglaciation of the North American Ice Sheet Complex. *Quaternary Science Reviews* **234**, 106223 (2020), doi:10.1016/j.quascirev.2020.106223, https://www.sciencedirect.com/science/article/pii/S0277379119307619.

28. A. S. Dyke, *et al.*, The Laurentide and Innuitian ice sheets during the Last Glacial Maximum. *Quaternary Science Reviews* **21** (1), 9–31 (2002), doi:10.1016/S0277-3791(01)00095-6, https://www.sciencedirect.com/science/article/pii/S0277379101000956.

29. A. S. Dyke, An outline of North American deglaciation with emphasis on central and northern Canada, in *Developments in Quaternary Sciences* (Elsevier), vol. 2, pp. 373–424 (2004), doi:10.1016/S1571-0866(04)80209-4, https://linkinghub.elsevier.com/retrieve/pii/S1571086604802094.

30. A. L. C. Hughes, R. Gyllencreutz, S. Lohne, J. Mangerud, J. I. Svendsen, The last Eurasian ice sheets – a chronological database and time-slice reconstruction, DATED-1. *Boreas* **45** (1), 1–

45 (2016), _eprint: https://onlinelibrary.wiley.com/doi/pdf/10.1111/bor.12142, doi:10.1111/bor.12142, https://onlinelibrary.wiley.com/doi/abs/10.1111/bor.12142.

31. T. P. M. Leger, *et al.*, A Greenland-wide empirical reconstruction of paleo ice sheet retreat informed by ice extent markers: PaleoGrIS version 1.0. *Climate of the Past* **20** (3), 701–755 (2024), doi:10.5194/cp-20-701-2024, https://cp.copernicus.org/articles/20/701/2024/.

32. K. Lambeck, A. Purcell, S. Zhao, The North American Late Wisconsin ice sheet and mantle viscosity from glacial rebound analyses. *Quaternary Science Reviews* **158**, 172–210 (2017), doi:10.1016/j.quascirev.2016.11.033, https://linkinghub.elsevier.com/retrieve/pii/S0277379116306047.

33. L. Tarasov, A. S. Dyke, R. M. Neal, W. R. Peltier, A data-calibrated distribution of deglacial chronologies for the North American ice complex from glaciological modeling. *Earth and Planetary Science Letters* **315-316**, 30–40 (2012), doi:10.1016/j.epsl.2011.09.010, https://www.sciencedirect.com/science/article/pii/S0012821X11005243.

34. C. R. Stokes, *et al.*, On the reconstruction of palaeo-ice sheets: Recent advances and future challenges. *Quaternary Science Reviews* **125**, 15–49 (2015), doi:10.1016/j.quascirev.2015.07.016, https://www.sciencedirect.com/science/article/pii/S027737911530055X.

35. K. Roy, W. Peltier, Glacial isostatic adjustment, relative sea level history and mantle viscosity: reconciling relative sea level model predictions for the U.S. East coast with geological constraints. *Geophysical Journal International* **201** (2), 1156–1181 (2015), doi:10.1093/gji/ggv066, http://academic.oup.com/gji/article/201/2/1156/579933/Glacial-isostatic-adjustment-relative-sea-level.

36. J. E. Tierney, *et al.*, Advances in Paleoclimate Data Assimilation. *Annual Review of Earth and Planetary Sciences* **53** (1), 625–650 (2025), doi:10.1146/annurev-earth-032320-064209, https://www.annualreviews.org/content/journals/10.1146/annurev-earth-032320-064209.

37. J. S. Drebber, C. T. Halsted, L. B. Corbett, P. R. Bierman, M. W. Caffee, In Situ Cosmogenic 10Be Dating of Laurentide Ice Sheet Retreat from Central New England, USA. *Geosciences* **13** (7), 213 (2023), doi:10.3390/geosciences13070213, https://www.mdpi.com/2076-3263/13/7/213.

38. B. Hall, T. Lowell, G. Bromley, A. Putnam, K. Allen, Rapid deglaciation of eastern Maine, northeastern North America, during Heinrich Stadial 1. *Quaternary Science Reviews* **363**, 109444 (2025), doi:10.1016/j.quascirev.2025.109444, https://www.sciencedirect.com/science/article/pii/S0277379125002641.

39. C. T. Halsted, *et al.*, Rapid southeastern Laurentide Ice Sheet thinning during the last deglaciation revealed by elevation profiles of in situ cosmogenic 10Be. *GSA Bulletin* (2022), doi:10.1130/B36463.1, https://pubs.geoscienceworld.org/gsabulletin/article/doi/10.1130/B36463.1/619399/Rapid-southeastern-Laurentide-Ice-Sheet-thinning.

40. A. Balter-Kennedy, *et al.*, The Laurentide Ice Sheet in southern New England and New York during and at the end of the Last Glacial Maximum: a cosmogenic-nuclide chronology. *Climate of the Past* **20** (9), 2167–2190 (2024), doi:10.5194/cp-20-2167-2024, https://cp.copernicus.org/articles/20/2167/2024/.

41. E. W. Portenga, D. J. Ullman, L. B. Corbett, P. R. Bierman, M. W. Caffee, Early Holocene ice retreat from Isle Royale in the Laurentian Great Lakes constrained with ^{10}Be exposure-age dating. *Geochronology* **5** (2), 413–431 (2023), doi:10.5194/gchron-5-413-2023, https://gchron.copernicus.org/articles/5/413/2023/.

42. P.-O. Couette, J.-F. Ghienne, P. Lajeunesse, J. Van der Woerd, Climatic control on the retreat of the Laurentide Ice Sheet margin in easternmost Québec–Labrador (Canada) revealed by cosmogenic nuclide exposure dating. *Journal of Quaternary Science* **38** (7), 1044–1061 (2023), doi:10.1002/jqs.3525, https://onlinelibrary.wiley.com/doi/abs/10.1002/jqs.3525.

879 43. N. E. Young, *et al.*, Late Holocene reexpansion of the Laurentide Ice Sheet. *Science*
880 **394** (6822), 455–459 (2026), doi:10.1126/science.aed3379, https://www.science.org/
881 doi/10.1126/science.aed3379.

882 44. M. Margold, C. R. Stokes, C. D. Clark, J. Kleman, Ice streams in the Laurentide Ice Sheet:
883 a new mapping inventory. *Journal of Maps* **11** (3), 380–395 (2015), doi:10.1080/17445647.
884 2014.912036, https://www.tandfonline.com/doi/full/10.1080/17445647.2014.
885 912036.

886 45. R. G. Fairbanks, A 17,000-year glacio-eustatic sea level record: influence of glacial melting
887 rates on the Younger Dryas event and deep-ocean circulation. *Nature* **342** (6250), 637–642
888 (1989), doi:10.1038/342637a0, https://www.nature.com/articles/342637a0.

889 46. L. J. Gregoire, A. J. Payne, P. J. Valdes, Deglacial rapid sea level rises caused by ice-sheet
890 saddle collapses. *Nature* **487** (7406), 219–222 (2012), doi:10.1038/nature11257, https:
891 //www.nature.com/articles/nature11257.

892 47. S. O. Rasmussen, *et al.*, A stratigraphic framework for abrupt climatic changes during
893 the Last Glacial period based on three synchronized Greenland ice-core records: refin-
894 ing and extending the INTIMATE event stratigraphy. *Quaternary Science Reviews* **106**,
895 14–28 (2014), doi:10.1016/j.quascirev.2014.09.007, https://www.sciencedirect.com/
896 science/article/pii/S0277379114003485.

897 48. R. B. Alley, A. M. Ágústsdóttir, The 8k event: cause and consequences of a ma-
898 jor Holocene abrupt climate change. *Quaternary Science Reviews* **24** (10), 1123–
899 1149 (2005), doi:10.1016/j.quascirev.2004.12.004, https://www.sciencedirect.com/
900 science/article/pii/S0277379105000314.

901 49. M. S. Gauthier, S. E. Kelley, T. J. Hodder, Lake Agassiz drainage bracketed Holocene
902 Hudson Bay Ice Saddle collapse. *Earth and Planetary Science Letters* **544**, 116372
903 (2020), doi:10.1016/j.epsl.2020.116372, https://www.sciencedirect.com/science/
904 article/pii/S0012821X20303162.

905 50. D. S. Kaufman, *et al.*, Holocene thermal maximum in the western Arctic (0–180°W).
906 *Quaternary Science Reviews* **23** (5), 529–560 (2004), doi:10.1016/j.quascirev.2003.09.007,
907 https://www.sciencedirect.com/science/article/pii/S0277379103002956.

908 51. R. L. HOOKE, H. B. CLAUSEN, Wisconsin and Holocene 18O variations, Barnes Ice
909 Cap, Canada. *GSA Bulletin* **93** (8), 784–789 (1982), doi:10.1130/0016-7606(1982)93⟨784:
910 WAHOVB⟩2.0.CO;2, https://doi.org/10.1130/0016-7606(1982)93%3C784:
911 WAHOVB%3E2.0.CO;2.

912 52. W. Dansgaard, J. W. C. White, S. J. Johnsen, The abrupt termination of the Younger Dryas
913 climate event. *Nature* **339** (6225), 532–534 (1989), doi:10.1038/339532a0, https://www.
914 nature.com/articles/339532a0.

915 53. R. B. Alley, *et al.*, Abrupt increase in Greenland snow accumulation at the end of the
916 Younger Dryas event. *Nature* **362** (6420), 527–529 (1993), doi:10.1038/362527a0, https:
917 //www.nature.com/articles/362527a0.

918 54. E. J. Gowan, L. Niu, G. Knorr, G. Lohmann, Geology datasets in North America, Green-
919 land and surrounding areas for use with ice sheet models. *Earth System Science Data*
920 **11** (1), 375–391 (2019), doi:10.5194/essd-11-375-2019, https://essd.copernicus.
921 org/articles/11/375/2019/.

922 55. J. D. Pelletier, *et al.*, A gridded global data set of soil, intact regolith, and
923 sedimentary deposit thicknesses for regional and global land surface model-
924 ing. *Journal of Advances in Modeling Earth Systems* **8** (1), 41–65 (2016),
925 _eprint: https://agupubs.onlinelibrary.wiley.com/doi/pdf/10.1002/2015MS000526, doi:
926 10.1002/2015MS000526, https://onlinelibrary.wiley.com/doi/abs/10.1002/
927 2015MS000526.

928 56. D. C. Barber, *et al.*, Forcing of the cold event of 8,200 years ago by catastrophic drainage of
929 Laurentide lakes. *Nature* **400** (6742), 344–348 (1999), doi:10.1038/22504, https://www.
930 nature.com/articles/22504.

931 57. C. T. Halsted, *et al.*, A critical re-analysis of constraints on the timing and rate of Laurentide Ice
932 Sheet recession in the northeastern United States. *Journal of Quaternary Science* **39** (1), 54–
933 69 (2024), _eprint: https://onlinelibrary.wiley.com/doi/pdf/10.1002/jqs.3563, doi:10.1002/jqs.
934 3563, https://onlinelibrary.wiley.com/doi/abs/10.1002/jqs.3563.

935 58. A. E. Carlson, *et al.*, Surface-melt driven Laurentide Ice Sheet retreat during the
936 early Holocene. *Geophysical Research Letters* **36** (24), 2009GL040948 (2009), doi:10.
937 1029/2009GL040948, https://agupubs.onlinelibrary.wiley.com/doi/10.1029/
938 2009GL040948.

939 59. S. Manabe, A. J. Broccoli, The influence of continental ice sheets on the climate of
940 an ice age. *Journal of Geophysical Research: Atmospheres* **90** (D1), 2167–2190 (1985),
941 _eprint: https://agupubs.onlinelibrary.wiley.com/doi/pdf/10.1029/JD090iD01p02167, doi:
942 10.1029/JD090iD01p02167, https://onlinelibrary.wiley.com/doi/abs/10.1029/
943 JD090iD01p02167.

944 60. J. Laskar, *et al.*, A long-term numerical solution for the insolation quantities of the Earth.
945 *Astronomy & Astrophysics* **428** (1), 261–285 (2004), doi:10.1051/0004-6361:20041335,
946 https://www.aanda.org/articles/aa/abs/2004/46/aa1335/aa1335.html.

947 61. E. Monnin, *et al.*, Atmospheric CO_2 Concentrations over the Last Glacial Termination. *Science*
948 **291** (5501), 112–114 (2001), doi:10.1126/science.291.5501.112, https://www.science.
949 org/doi/10.1126/science.291.5501.112.

950 62. K. M. Cuffey, G. D. Clow, Temperature, accumulation, and ice sheet el-
951 evation in central Greenland through the last deglacial transition. *Journal*
952 *of Geophysical Research: Oceans* **102** (C12), 26383–26396 (1997), _eprint:
953 https://agupubs.onlinelibrary.wiley.com/doi/pdf/10.1029/96JC03981, doi:10.1029/
954 96JC03981, https://onlinelibrary.wiley.com/doi/abs/10.1029/96JC03981.

955 63. M. B. Osman, *et al.*, Globally resolved surface temperatures since the Last Glacial Max-
956 imum. *Nature* **599** (7884), 239–244 (2021), doi:10.1038/s41586-021-03984-4, https:
957 //www.nature.com/articles/s41586-021-03984-4.

64. S. L. Heath, H. M. Loope, B. B. Curry, T. V. Lowell, Pattern of southern Laurentide Ice Sheet margin position changes during Heinrich Stadials 2 and 1. *Quaternary Science Reviews* **201**, 362–379 (2018), doi:10.1016/j.quascirev.2018.10.019, https://linkinghub.elsevier.com/retrieve/pii/S0277379118303779.

65. D. J. Ullman, A. N. LeGrande, A. E. Carlson, F. S. Anslow, J. M. Licciardi, Assessing the impact of Laurentide Ice Sheet topography on glacial climate. *Climate of the Past* **10** (2), 487–507 (2014), doi:10.5194/cp-10-487-2014, https://cp.copernicus.org/articles/10/487/2014/.

66. J. F. McManus, R. Francois, J.-M. Gherardi, L. D. Keigwin, S. Brown-Leger, Collapse and rapid resumption of Atlantic meridional circulation linked to deglacial climate changes. *Nature* **428** (6985), 834–837 (2004), doi:10.1038/nature02494, https://www.nature.com/articles/nature02494.

67. J. A. Badgeley, E. J. Steig, G. J. Hakim, T. J. Fudge, Greenland temperature and precipitation over the last 20 000 years using data assimilation. *Climate of the Past* **16** (4), 1325–1346 (2020), doi:10.5194/cp-16-1325-2020, https://cp.copernicus.org/articles/16/1325/2020/.

68. S. Hinck, E. J. Gowan, X. Zhang, G. Lohmann, PISM-LakeCC: Implementing an adaptive proglacial lake boundary in an ice sheet model. *The Cryosphere* **16** (3), 941–965 (2022), doi:10.5194/tc-16-941-2022, https://tc.copernicus.org/articles/16/941/2022/.

69. A. J. Koester, *et al.*, Rapid thinning of the Laurentide Ice Sheet in coastal Maine, USA, during late Heinrich Stadial 1. *Quaternary Science Reviews* **163**, 180–192 (2017), doi:10.1016/j.quascirev.2017.03.005, https://www.sciencedirect.com/science/article/pii/S0277379116305273.

70. S. L. Norris, M. Margold, D. J. A. Evans, N. Atkinson, D. G. Froese, Dynamical response of the southwestern Laurentide Ice Sheet to rapid Bølling–Allerød warming. *The Cryosphere* **18** (4), 1533–1559 (2024), doi:10.5194/tc-18-1533-2024, https://tc.copernicus.org/articles/18/1533/2024/.

71. D. J. Ullman, *et al.*, Final Laurentide ice-sheet deglaciation and Holocene climate-sea level change. *Quaternary Science Reviews* **152**, 49–59 (2016), doi:10.1016/j.quascirev.2016.09.014, https://www.sciencedirect.com/science/article/pii/S027737911630364X.

72. A. Dyke, V. Prest, Late Wisconsinan and Holocene History of the Laurentide Ice Sheet. *Géographie physique et Quaternaire* **41** (2), 237–263 (1987), doi:10.7202/032681ar, https://www.erudit.org/en/journals/gpq/1987-v41-n2-gpq1945/032681ar/.

73. B. J. Stoker, *et al.*, Ice flow dynamics of the northwestern Laurentide Ice Sheet during the last deglaciation. *The Cryosphere* **19** (2), 869–910 (2025), doi:10.5194/tc-19-869-2025, https://tc.copernicus.org/articles/19/869/2025/.

74. J. T. Andrews, B. MacLean, Hudson Strait ice streams: a review of stratigraphy, chronology and links with North Atlantic Heinrich events. *Boreas* **32** (1), 4–17 (2003), _eprint: https://onlinelibrary.wiley.com/doi/pdf/10.1080/03009480310001010, doi:10.1080/03009480310001010, https://onlinelibrary.wiley.com/doi/abs/10.1080/03009480310001010.

75. S. R. Hemming, Heinrich events: Massive late Pleistocene detritus layers of the North Atlantic and their global climate imprint doi:10.1029/2003RG000128, https://agupubs.onlinelibrary.wiley.com/doi/10.1029/2003RG000128.

76. C. L. Batchelor, *et al.*, Rapid, buoyancy-driven ice-sheet retreat of hundreds of metres per day. *Nature* **617** (7959), 105–110 (2023), doi:10.1038/s41586-023-05876-1, https://www.nature.com/articles/s41586-023-05876-1.

77. G. J. G. Paxman, J. Austermann, K. J. Tinto, A fault-bounded palaeo-lake basin preserved beneath the Greenland Ice Sheet. *Earth and Planetary Science Letters* **553**, 116647 (2021), doi:10.1016/j.epsl.2020.116647, https://www.sciencedirect.com/science/article/pii/S0012821X20305914.

78. B. Kulessa, *et al.*, Seismic evidence for complex sedimentary control of Greenland Ice Sheet flow. *Science Advances* **3** (8), e1603071 (2017), doi:10.1126/sciadv.1603071, https://www.science.org/doi/full/10.1126/sciadv.1603071.

79. A. J. Christ, *et al.*, A multimillion-year-old record of Greenland vegetation and glacial history preserved in sediment beneath 1.4 km of ice at Camp Century. *Proceedings of the National Academy of Sciences* **118** (13), e2021442118 (2021), doi:10.1073/pnas.2021442118, https://www.pnas.org/doi/abs/10.1073/pnas.2021442118.

80. F. Walter, J. Chaput, M. P. Lüthi, Thick sediments beneath Greenland's ablation zone and their potential role in future ice sheet dynamics. *Geology* **42** (6), 487–490 (2014), doi:10.1130/G35492.1, https://doi.org/10.1130/G35492.1.

81. G. H. Miller, A. S. Dyke, Proposed Extent of Late Wisconsin Laurentide Ice on Eastern Baffin Island. *Geology* **2** (3), 125–130 (1974), doi:10.1130/0091-7613(1974)2⟨125:PEOLWL⟩2.0.CO;2, https://doi.org/10.1130/0091-7613(1974)2<125:PEOLWL>2.0.CO;2.

82. N. E. Young, J. P. Briner, D. H. Rood, R. C. Finkel, Glacier Extent During the Younger Dryas and 8.2-ka Event on Baffin Island, Arctic Canada. *Science* **337** (6100), 1330–1333 (2012), doi:10.1126/science.1222759, https://www.science.org/doi/10.1126/science.1222759.

83. M. S. Gauthier, A. Breckenridge, T. J. Hodder, Patterns of ice recession and ice stream activity for the MIS 2 Laurentide Ice Sheet in Manitoba, Canada. *Boreas* **51** (2), 274–298 (2022), doi:10.1111/bor.12571, https://onlinelibrary.wiley.com/doi/abs/10.1111/bor.12571.

84. Government of Saskatchewan, Surficial geology 1M (2019), https://geohub.saskatchewan.ca/datasets/saskatchewan::surficial-geology-1m-1/about.

85. M. M. Fenton, *et al.*, Surficial geology of Alberta. *Alberta Energy Regulator, AER/AGS Map* **601** (1), 1–000 (2013).

86. K. Roy, W. Peltier, Relative sea level in the Western Mediterranean basin: A regional test of the ICE-7G_NA (VM7) model and a constraint on late Holocene Antarctic deglacia-

tion. *Quaternary Science Reviews* **183**, 76–87 (2018), doi:10.1016/j.quascirev.2017.12.021, https://linkinghub.elsevier.com/retrieve/pii/S027737911730642X.

87. U. Mukherjee, *et al.*, Sea-level rise at the end of the last deglaciation dominated by North American ice sheets. *Nature Geoscience* **18** (11), 1167–1173 (2025), doi:10.1038/s41561-025-01806-0, https://www.nature.com/articles/s41561-025-01806-0.

88. O. Abril-Pla, *et al.*, PyMC: a modern, and comprehensive probabilistic programming framework in Python. *PeerJ Computer Science* **9**, e1516 (2023), doi:10.7717/peerj-cs.1516, https://peerj.com/articles/cs-1516.

89. Y. Lin, *et al.*, PaleoSTeHM v1.0: a modern, scalable spatiotemporal hierarchical modeling framework for paleo-environmental data. *Geoscientific Model Development* **18** (9), 2609–2637 (2025), doi:10.5194/gmd-18-2609-2025, https://gmd.copernicus.org/articles/18/2609/2025/.

90. E. L. Ashe, N. S. Khan, L. T. Toth, A. Dutton, R. E. Kopp, A statistical framework for integrating nonparametric proxy distributions into geological reconstructions of relative sea level. *Advances in Statistical Climatology, Meteorology and Oceanography* **8** (1), 1–29 (2022), doi:10.5194/ascmo-8-1-2022, https://ascmo.copernicus.org/articles/8/1/2022/.

91. C. E. Rasmussen, C. K. I. Williams, *Gaussian processes for machine learning*, Adaptive computation and machine learning (MIT Press, Cambridge, Mass.), 3. print ed. (2008).

92. B. Dyer, *et al.*, Sea-level trends across The Bahamas constrain peak last interglacial ice melt. *Proceedings of the National Academy of Sciences* **118** (33), e2026839118 (2021), doi:10.1073/pnas.2026839118, https://pnas.org/doi/full/10.1073/pnas.2026839118.

93. D. R. Soller, P. H. Packard, C. P. Garrity, *Database for USGS Map I-1970 - Map showing the thickness and character of Quaternary sediments in the glaciated United States east of the Rocky Mountains*, Tech. Rep. 656, U.S. Geological Survey (2012), doi:10.3133/ds656, https://pubs.usgs.gov/publication/ds656, publication Title: Data Series.

94. M. S. Gauthier, *et al.*, Extending the western Hudson Bay Lowland Quaternary stratigraphy, in Manitoba Canada, to at least Marine Isotope Stage 10.

Canadian Journal of Earth Sciences **63**, 1 (2025), doi:10.1139/cjes-2025-0027, https://openurl.ebsco.com/contentitem/doi:10.1139%2Fcjes-2025-0027?sid=ebsco:plink:crawler&id=ebsco:doi:10.1139%2Fcjes-2025-0027.

95. W. W. Shilts, Chapter 4 Glaciation of the Hudson Bay Region, in *Canadian Inland Seas*, I. P. Martini, Ed. (Elsevier), vol. 44 of *Elsevier Oceanography Series*, pp. 55–78 (1986), doi:10.1016/S0422-9894(08)70897-3, https://www.sciencedirect.com/science/article/pii/S0422989408708973.

96. I. Joughin, S. Tulaczyk, Positive Mass Balance of the Ross Ice Streams, West Antarctica. *Science* **295** (5554), 476–480 (2002), doi:10.1126/science.1066875, https://www.science.org/doi/full/10.1126/science.1066875.

97. W. Richard Peltier, D. F. Argus, R. Drummond, Comment on "An Assessment of the ICE-6G_C (VM5a) Glacial Isostatic Adjustment Model" by Purcell et al. *Journal of Geophysical Research: Solid Earth* **123** (2), 2019–2028 (2018), doi:10.1002/2016JB013844, https://onlinelibrary.wiley.com/doi/abs/10.1002/2016JB013844.

98. S. L. Norris, *et al.*, Rapid retreat of the southwestern Laurentide Ice Sheet during the Bølling-Allerød interval. *Geology* **50** (4), 417–421 (2021), doi:10.1130/G49493.1, https://doi.org/10.1130/G49493.1.

99. J. Gosse, *et al.*, Using Cosmogenic Isotopes to Interpret the Landscape Record of Glaciation: Nunataks in Newfoundland?, in *Glacier Science and Environmental Change* (John Wiley & Sons, Ltd), pp. 442–446 (2006), doi:10.1002/9780470750636.ch89, https://onlinelibrary.wiley.com/doi/abs/10.1002/9780470750636.ch89, section: Eighty-Nine _eprint: https://onlinelibrary.wiley.com/doi/pdf/10.1002/9780470750636.ch89.

100. D. J. A. Evans, C. D. Clark, B. R. Rea, Landform and sediment imprints of fast glacier flow in the southwest Laurentide Ice Sheet. *Journal of Quaternary Science* **23** (3), 249–272 (2008), doi:10.1002/jqs.1141, https://onlinelibrary.wiley.com/doi/abs/10.1002/jqs.1141.

101. C. D. Clark, J. K. Knight, J. T. Gray, Geomorphological reconstruction of the Labrador Sector of the Laurentide Ice Sheet. *Quaternary Science Reviews* **19** (13), 1343–1366 (2000), doi:10.1016/S0277-3791(99)00098-0, https://www.sciencedirect.com/science/article/pii/S0277379199000980.

102. E. Nielsen, *et al.*, Stratigraphy, paleoecology, and glacial history of the Gillam area, Manitoba. *Canadian Journal of Earth Sciences* **23** (11), 1641–1661 (1986), doi:10.1139/e86-153, http://www.nrcresearchpress.com/doi/10.1139/e86-153.

103. L. H. Thorleifson, P. H. Wyatt, W. W. Shilts, E. Nielsen, Hudson Bay lowland Quaternary stratigraphy: Evidence for early Wisconsinan glaciation centered in Quebec, in *The Last Interglacial-Glacial Transition in North America*, P. U. Clark, P. D. Lea, Eds. (Geological Society of America), p. 0 (1992), doi:10.1130/SPE270-p207, https://doi.org/10.1130/SPE270-p207.

104. T. J. Hodder, *et al.*, Unravelling the fragmented sediment–landform assemblage in an area of thick Quaternary sediment, western Hudson Bay Lowland, Canada. *Canadian Journal of Earth Sciences* **61** (11), 1156–1183 (2024), doi:10.1139/cjes-2024-0018, https://doi.org/10.1139/cjes-2024-0018.

105. A. S. Dalton, S. A. Finkelstein, P. J. Barnett, S. L. Forman, Constraining the Late Pleistocene history of the Laurentide Ice Sheet by dating the Missinaibi Formation, Hudson Bay Lowlands, Canada. *Quaternary Science Reviews* **146**, 288–299 (2016), doi:10.1016/j.quascirev.2016.06.015, https://www.sciencedirect.com/science/article/pii/S0277379116302153.

106. J. Kleman, *et al.*, North American Ice Sheet build-up during the last glacial cycle, 115–21 kyr. *Quaternary Science Reviews* **29** (17), 2036–2051 (2010), doi:10.1016/j.quascirev.2010.04.021, https://www.sciencedirect.com/science/article/pii/S0277379110001307.

107. H. W. Josenhans, J. Zevenhuizen, Dynamics of the Laurentide Ice Sheet in Hudson Bay, Canada. *Marine Geology* **92** (1), 1–26 (1990), doi:10.1016/0025-3227(90)90024-E, https://www.sciencedirect.com/science/article/pii/002532279090024E.

108. N. Eyles, J. I. Boyce, R. W. Barendregt, Hummocky moraine: sedimentary record of stagnant Laurentide Ice Sheet lobes resting on soft beds. *Sedimentary Geology* **123** (3), 163–174 (1999), doi:10.1016/S0037-0738(98)00129-8, https://www.sciencedirect.com/science/article/pii/S0037073898001298.

109. K. M. Syverson, P. M. Colgan, The Quaternary of Wisconsin: A review of stratigraphy and glaciation history, in *Quaternary Glaciations-Extent and Chronology*, J. Ehlers, P. L. Gibbard, Eds. (Elsevier), vol. 2 of *Developments in Quaternary Sciences*, pp. 295–311 (2004), doi:10.1016/S1571-0866(04)80205-7, https://www.sciencedirect.com/science/article/pii/S1571086604802057.

110. D. R. Soller, P. H. Packard, *Digital representation of a map showing the thickness and character of Quaternary sediments in the glaciated United States east of the Rocky Mountains*, Tech. Rep. 38, The Survey ; For sale by USGS Information Services, (1998), doi:10.3133/ds38, https://pubs.usgs.gov/publication/ds38, publication Title: Data Series.

111. P. R. Bierman, K. A. Marsella, C. Patterson, P. T. Davis, M. Caffee, Mid-Pleistocene cosmogenic minimum-age limits for pre-Wisconsinan glacial surfaces in southwestern Minnesota and southern Baffin Island: a multiple nuclide approach. *Geomorphology* **27** (1), 25–39 (1999), doi:10.1016/S0169-555X(98)00088-9, https://www.sciencedirect.com/science/article/pii/S0169555X98000889.

112. J. Clark, *et al.*, The age of the opening of the Ice-Free Corridor and implications for the peopling of the Americas. *Proceedings of the National Academy of Sciences* **119** (14), e2118558119 (2022), doi:10.1073/pnas.2118558119, https://www.pnas.org/doi/abs/10.1073/pnas.2118558119.

113. M. Margold, *et al.*, Beryllium-10 dating of the Foothills Erratics Train in Alberta, Canada, indicates detachment of the Laurentide Ice Sheet from the Rocky Mountains at ˜15 ka. *Quaternary Research* **92** (2), 469–482 (2019), doi:10.1017/qua.2019.10, https://www.cambridge.org/core/journals/quaternary-research/article/abs/beryllium10-dating-of-the-foothills-erratics-train-in-alberta-canada-indicates-de
DA75A7DEBB2FC2B214F6B9CFA68B26C4.

114. M. MacFerrin, C. Amante, K. Carignan, M. Love, E. Lim, The Earth Topography 2022 (ETOPO 2022) global DEM dataset. *Earth System Science Data* **17** (5), 1835–1849 (2025), doi:10.5194/essd-17-1835-2025, https://essd.copernicus.org/articles/17/1835/2025/.

Acknowledgments

Funding: SJC and JA were supported by the SWAIS2C grant (OPP 2034719). RC was supported by a Woods Hole Oceanographic Institution Postdoctoral Scholarship and Texas A&M start up funding. NEY was supported by NSF-OPP award #2416598.

Author contributions: Conceptualization: S.J.C., J.A., R.C.C. Data Curation: S.J.C., B.J.S., N.E.Y. Formal Analysis: S.J.C. Investigation: S.J.C. Funding Acquisition: J.A. Methodology: S.J.C., J.A., B.J.S., R.C.C., B.D. Visualization: S.J.C. Supervision: J.A., W.J.D. Writing—original draft: S.J.C. Writing—review & editing: All authors.

Competing interests: The authors declare they have no competing interests.

Data and materials availability: All code and algorithms used in this study to generate the ALIS reconstruction, conduct analysis, and produce visualizations are openly available for transparency and reproducibility. The source code along with files containing the gridded ALIS posterior—median and 95% CI—are available in the Dryad repository accompanying this manuscript. The North American geochronological datasets from (*9*) updated with recent TCN data from (*37–43*), the geomorphic datasets from (*5, 44, 54, 55, 70, 73, 81, 83–85*), and the pipelines to combine and format them, are available in the repository for reproducibility. The ice sheet reconstructions from (*32, 86, 87*) used in the prior ensemble are also included in the repository. This study did not generate any new materials.

AI Declaration: ChatGPT-5 and Claude Sonnet 4.6 were used for limited assistance with coding tasks, including debugging, file reformatting, cartographic reprojection, and formatting code to generate figures and visualizations; all code was tested and validated by the authors.

Supplementary materials

Supplementary Text

Figs. S1 to S11

Tables S1

Caption for Movie S1

References *(97-114)*

Supplementary Materials for

Climatic and ice dynamic controls on the deglaciation of the Laurentide Ice Sheet

Samuel J. Chester*, Jacqueline Austermann, Benjamin J. Stoker, Roger C. Creel,
William J. D'Andrea, Blake Dyer, Nicolás E. Young, April S. Dalton
*Corresponding author. Email: schester@ldeo.columbia.edu

This PDF file includes:

Supplementary Text
Figures S1 to S11
Table S1
Caption for Movie S1

Supplementary Material

Additional datasets and constraints

We updated the NADD from (*9*) with additional TCN constraints published since its release (*37–42*). We follow the screening protocol and methodology for calculating exposure ages exactly as described in (*9*). In brief, we calculated ^{10}Be exposure ages using the *expage* calculator version 201912 (https://expage.github.io/calculator). Ages are corrected for glacial isostatic adjustment using the ANU model (*32*)—or ICE-6G model if the sample is west of 140° W or east of 60 ° W (*97*). Outliers identified by the original authors were excluded from the feature or site age. The youngest and oldest age of the data set were assigned the minimum and maximum age of the feature, respectively, and the age of the feature is the simple average of calculated ages. Sites/features with less than two measurements were excluded. See (*9*) for a detailed description of TCN age calculation. The treatment of these ages in the ALIS reconstruction then follows as described in the Methods. The one exception is for the ages and uncertainties of the Martha's Vineyard, Buzzard's Bay, Old Saybrook, and Ledyard, Ronkonkoma, and Roanoke Moraines (Table S1). For these features, we incorporate the preferred ages and uncertainties based on the production rate calculations and careful interpretations of the authors (*40*).

A few other minor adjustments were made to NADD in addition to those described in the methods. Two radiocarbon ages that are incorrectly labeled 'minimum' times for deglaciation in NADD (and the supplement of the referenced publication, (*64*)) were corrected to reflect 'maximum ages'. These are UCIAMS-97068 and UCIAMS-97039. We also remove two ages from basal sediment in cores taken offshore in Baffin Bay, far from the lateral extent of the LIS: ETH-58355.1.1 and CURL18628.

Two TCN-dated features included in NADD are also removed. The first is the 'Beaver River Region' feature originally published in (*98*) as these ages date a gravel bar that should be interpreted as the formation of the fluvial feature rather than exposure following ice retreat. The second is a nunatak in Newfoundland from (*99*) because this is primarily related to ice thinning rather than the lateral extent of the ice margin.

The six major ice caps in the Canadian Arctic, including the last remnant of the Laurentide—the Barnes Ice Cap (BIC)—are represented similar to the 'advance' radiocarbon ages with an assigned

age of 5 ka and 'measurement' uncertainty of one hundred years. In practice, this enforces that ice must still be around by 5 ka, roughly the final demise of the LIS and the time period of interest in this study. Note that many of these ice caps have spatially complex margins that contour fjorded topography, and thus it is beyond the ability of this lower resolution reconstruction to replicate these margins exactly.

We supplement the moraine dataset with nine additional moraines. Two are from the northwestern sector and are undated (*73*). One is a generalized mapping of the Cockburn Moraine on Baffin Island (*81*). Previous work has shown that discontinuous moraines at the fjord heads on Baffin Island have the same age, forming during the same climatic event, and are thus mapped as one continuous moraine (*5*). The moraine is assigned the corresponding age following (*9*), who originally only correlated the age with a shorter-length moraine set. Four additional moraines are from (*83*) and include the South Knife, Sipiwesk, and George Island moraines, as well as one unnamed moraine. Finally the Thompson Lake and Lethbridge moraines used in the regional reconstruction of (*70*) were included. We mapped these features from the Alberta and Saskatchewan provincial surficial geologic maps (*84, 85*), cross referenced to the mapping of (*70, 100*). Two moraines related to a small region in Minnesota that was never glaciated—Alexandria and St. Croix Moraines—are removed as they are beyond the resolving power of the model.

Notes on ice sheet priors

The ice sheet models in our ensemble were converted from three-dimensional fields of ice thickness change to two-dimensional latitude-longitude grids of deglaciation time by taking the last (youngest) time at which ice thickness at each grid cell goes to zero. Areas beyond the extent of the modeled ice sheet are assigned an age corresponding to the maximum age of retreat at the LGM margin for the given model. The ice sheet models generally have time steps of 500 or 1000 yrs, so the deglacial field has sharp and unrealistic contours. We remove these by applying a smoothing Gaussian filter.

Notes on Bayesian Modeling

The formal definition of the split-normal distributions for our data is:

$$p(y_i \mid f_i, \sigma_{L,i}, \sigma_{R,i}) = \frac{2}{(\sigma_{L,i} + \sigma_{R,i})\sqrt{2\pi}} \exp\left[-\frac{1}{2}\left(\frac{y_i - f_i}{\sigma_{L,i}}\right)^2\right] \quad \text{for } y_i < f_i, \tag{S1}$$

and analogously with $\sigma_{R,i}$ for $y_i \geq f_i$. Here, f_i is the predicted 'true' value at location i, and $\sigma_{H,i}$ and $\sigma_{L,i}$ are the high and low 1-sigma uncertainties.

Differences between the ALIS and NADI-1 reconstructions

Here, we review notable differences the NADI-1 and ALIS reconstruction. Differences between the NADI-1 and ALIS arise for three primary reasons: 1) treatment of minimum-limiting data, 2) geomorphic data not included in the ALIS and 3) spatial resolution. We review each of these below and provide examples, highlight all of the notable differences between the two reconstructions.

In many regions under the former LIS, the only available geochronological constraints are minimum-limiting radiocarbon ages with little or no indication of the elapsed time since deglaciation (lag time). Previous studies acknowledge this challenge, but still often rely on these ages to draw paleo margins. In some cases, this uncertainty is accounted for by drawing 'minimum' and 'maximum' margins, but the 'optimum' margins may still be biased. The ALIS model offers a new mechanism to quantify uncertainty related to these limiting constraints. In doing so, the average margin position predicted by ALIS reflects this possibility of earlier deglaciation and thus differs from the previous reconstructions in regions with only minimum-limiting constraints. Notable locations include Canadian Arctic Archipelago (Innuitian Ice Sheet), the Hudson Strait, marine-terminating areas of the LIS LGME, and the final stages of the Keewatin and Labrador Domes. In these locations, the ALIS median deglaciation is up to kyrs older than the NADI-1 optimal reconstruction, but also often with large posterior uncertainties (Fig. S7). Also notably older than the NADI-1 is the unzipping of the ice-free corridor between the CIS and the LIS. While the western side of the corridor is well dated by TCN ages, the eastern side of the central and southern suture zone is only constrained with radiocarbon ages (Fig. 1). Accordingly, the ALIS predicts unzipping finishing at 14.4 ka (14.9-13.8 ka 95% CI), which is over a thousand years earlier than the NADI-1 (Fig. S9). However, to the north, where TCN ages constrain the LIS side of the suture zone, the ALIS is in better agreement with previous studies (*9, 24*). Another discrepancy is in Manitoba, Canada, where previous authors have identified conflicting geochronological evidence

in two separate areas (c.f. (*9*), section 4.4.3: "Difficulties in merging disparate ice margins"). Here, the ALIS more closely reflects a deglacial scenario following the TCN dated Cree Lake Moraine (e.g. (*98*), rather than evidence from stratigraphic analysis and radiocarbon dating of marine and freshwater shells (*83*). While this scenario differs from the optimal margin positions in NADI-1, it falls within the minimum and maximum bounds which reflect the geologic discrepancy. These discrepancies highlight possibly unaccounted-for sources of uncertainty in previous margin reconstructions that we attempt to acknowledge and quantify in ALIS. While we took a conservative approach to modeling minimum-limiting radiocarbon ages by allowing for very large lag times (see 4), the data assimilation model offers a new tool for future researchers to assess the impact of more nuanced interpretations of radiocarbon ages, e.g. model ages with predetermined lag times, or a specific range of possible lag times. In data-dense regions, lag times could even be inferred as learned hyperparameters in a Bayesian framework.

The second reason for discrepancies relates to geomorphic data not currently included in the ALIS reconstruction. Evidence for paleo-ice flow during the deglacial including eskers, bedrock striations and mapped flow sets, help constrain the margin geometry in NADI-1 where direct chronological constraints are unavailable. For example, the breakup of the Labrador Dome in the NADI-1 reflects interpretations from mapped flow sets across Labrador and Quebec ('Scenario C' in (*101*)), while in the ALIS reconstruction the margins mirrors the geometry of the ice sheet prior (Fig. S7). Future work may seek to include these geomorphic datasets in the Bayesian framework similar to the current treatment of ice streams or moraines, however this is beyond the scope of the current study.

Finally, the ALIS is limited to a constant and fairly-coarse spatial resolution across the entire domain while the NADI-1 reflects mapping on a range of spatial scales given the available constraints. This results in differences where the margin had a complex geometry, for example ice lobes in the US Midwest and fjorded regions such as coastal Baffin Island and Labrador (Fig. S7). However, these small-scale limitations are of less importance in deriving broad-scale drivers of retreat across the termination. Similar to the resolution issue, the ALIS cannot resolve the build up phase to the LGME or local readvances during deglaciation. This leads to apparent discrepancies particularly during the early deglaciation where the ALIS appears to reflect a large LIS that may in fact be smaller due to the advancing ice towards to the LGME (e.g. the Northwest Margin of the

LIS; Fig. S7. This motivated our analysis of deglacial retreat rates rather than absolute size of the LIS over the deglaciation.

These differences highlight the complementary nature of the two approaches. Mapping based reconstructions can infer margins with high spatial resolution where data allows and benefit from the inclusion of many data types reconciled with expert knowledge, while the statistical approach provides a framework to apply consistent treatment of chronological constraints and infer spatially continuous fields with quantified uncertainties.

The representation of uncertainty in ALIS versus NADI-1

An interesting difference between ALIS and NADI-1 is related to the fundamental concept of how uncertainty is represented in different dimensions. The ALIS provides point wise uncertainty across North America, while the NADI-1 provides minimum and maximum margin positions that are then used to generate 1D transects that show the deviation of the min/max margins from the optimal through time. This serves as a way to assess how well-constrained the margin is at a given time, however it does not take into account how quickly the margin itself is moving. For example, if the optimal position moves a thousand kilometers in 1 kyr, and the min/max show the same shift in margin position but offset by +/- 0.5 kyr, then it may appear as though there is large uncertainty in the margin; it could span a distance of 2000 kilometers at any one time. However, an alternative way to understand this uncertainty is that over this large region, we actually know the deglaciation age to within 1 kyr. Taking the opposite scenario, a margin that migrates only a 100 kilometers but whose max and min allow for +/- 2 kyr, will appear as though only small deviations in position are possible over time, but at any given location along the transect the deglaciation age can range over 4 kyr. This highlights the fundamental difference between how uncertainty is understood in the transect approach in NADI-1 compared to the point-wise uncertainty from the ALIS posterior. We argue that ALIS provides a more interpretable quantification as it is simply the uncertainty in deglaciation at the given location. Incorporated in this quantification is the observation noted above that for the same amount of data, a stable margin with a longer residence time in a given area is harder to constrain than a margin that migrates rapidly; for example as the margin migrates north of the St. Lawrence and slows in southern Labrador, posterior uncertainties increase despite data

constraints in the region (Fig. 2).

Sediment distribution across North America

It is challenging to assess the exact subglacial conditions of the Laurentide ice sheet during the deglaciation. Here, we used the sediment thickness map of (*55*) as a proxy for subglacial conditions. This reconstruction includes some post-glacial sediment either from glacial outwash, proglacial lakes, or marine deposition. It is challenging to disentangle the pre- from the post-glacial, however, we believe this reconstruction is still a reasonable proxy at large scale for the subglacial conditions experienced by the Laurentide Ice Sheet for two reasons.

First, there is direct evidence that the LIS overlaid large sedimentary deposits in regions indicated by the (*55*) reconstruction. Regarding the Hudson Bay Lowlands region identified by the reviewer, there is extensive evidence for thick pre-Holocene deposits often lumped in to the 'Missinaibi Formation' that include tills from multiple glaciations as well as inter-till lacustrine and fluvial deposits going back as far as MIS 10 (*49, 94, 95, 102–105*). These sequences are tens of meters in thickness in many localities, while the overlying Holocene deposits are on the order of meters. The extent of these sequences has been mapped to a similar lateral extent as the thick deposits in the (*55*) dataset [c.f. (*95, 103*). The stratigraphic information contained in these deposits is a key constraint in understanding the LGM buildup of the LIS (*106*) and certainly represent a broad region of soft sediment basal conditions under the LIS as it deglaciated. Sonar data have been used to correlate these deposits with pre-Holocene sediment in the modern Hudson Bay as well (*107*). Regarding the thick sediment near the periphery of the LIS (beyond the Canadian Shield), these deposits agree well with the soft-bedded regions reconstructed in (*72*) [c.f. (*72*) Fig 3, Zone 1] and investigated by other researchers (*108, 109*). Additionally, an independent surficial geology map showing Quaternary sediment thickness across the Northern U.S. [southern LIS; (*110*)) shows good agreement with the (*55*) dataset with the thickest deposits under the James and Des Moines Lobes and south of Lake Michigan, while deposits are significantly thinner along the LIS LGM extent to the west in Montana and to the east in Pennsylvania, New Jersey and New York. In the US Midwest, the extensive tills of the most recent glaciation are also underlain by pre-Wisconsinan tills and inter-till deposits in many places (*109, 111*).

Table S1: **Updated deglaciation ages and uncertainties for southeast Laurentide Ice Sheet moraines.** Deglaciation ages and associated uncertainties are from (*40*).

Moraine	Age (ka)	Uncertainty (ka)
Martha's Vineyard Moraine	25.4	±2.5
Buzzard's Bay Moraine	22.2	±0.8
Old Saybrook Moraine	21.1	±0.8
Ledyard Moraine	21.0	±0.8
Ronkonkoma Moraine	22.4	±0.8
Roanoke Moraine	22.2	±0.8

Second, the pattern of deglacial sediment in (*55*) is consistent with a map of sediment cover distribution across North America from (*54*), which we also used along with two other maps of bedrock and surficial geology from the same study in our analysis to add confidence to our results (Fig. 3). These reconstructions provide 1) the distribution of sediment cover (continuous, veneer or dominantly bedrock), 2) the average grain size of the sediment, and 3) the bedrock geology type. The datasets were compiled specifically for use as a subglacial boundary conditions in ice sheet model simulations at '5 km or greater' resolution (*54*) and thus we consider it a good dataset to compare to the ALIS reconstruction. Where the late Wisconsin till is buried either by post-glacial sediment or modern lakes/oceans, the original authors looked to published records to estimate the sediment type and properties below the Holocene sections (*54*). The ALIS reconstruction compared to these datasets is presented in Fig. 3H. The percent of the LIS margin along 'continuous sediment cover' over time tracks very closely to the average sediment thickness along the margin over time calculated using (*55*). We would expect continuous cover to correlate with thick sedimentary deposits, so we believe this adds confidence in our findings regarding the relationship between retreat rates and bed conditions.

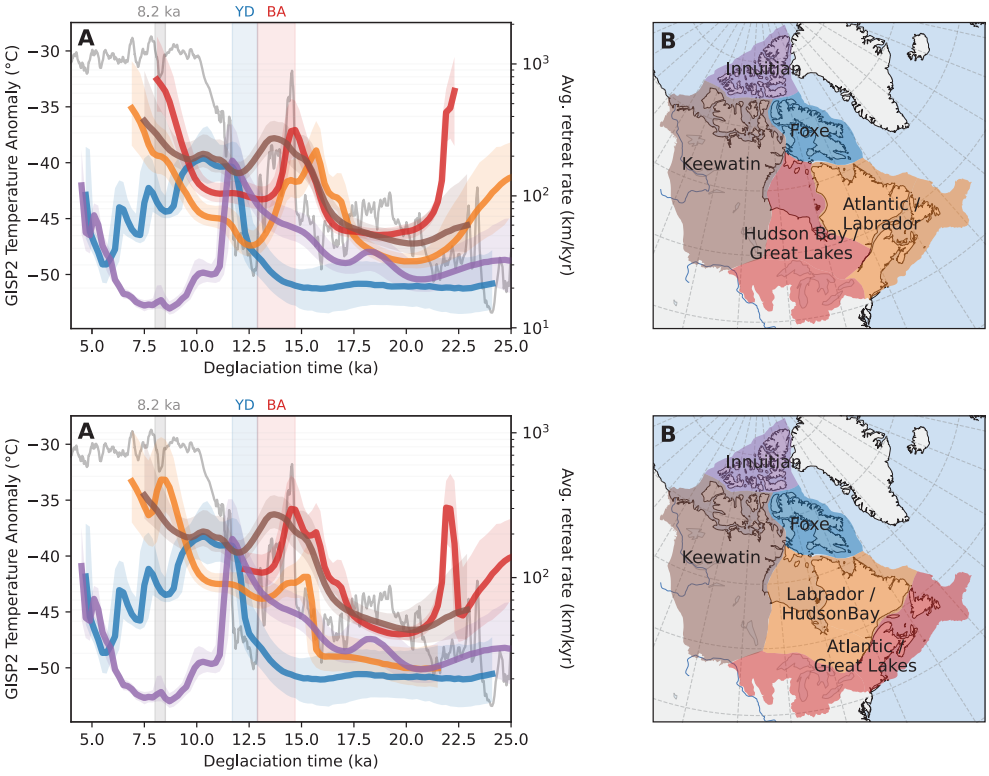


Figure S1: **Sensitivity of regional analysis of retreat rates to region delineation.** Average retreat rates (RR) for each region are calculated as in Fig. 4, but with combined Atlantic-Labrador and Hudson Bay-Great Lakes regions (**A**,**B**) and combined Labrador-Hudson Bay and Atlantic-Great Lakes regions (**C**,**D**).

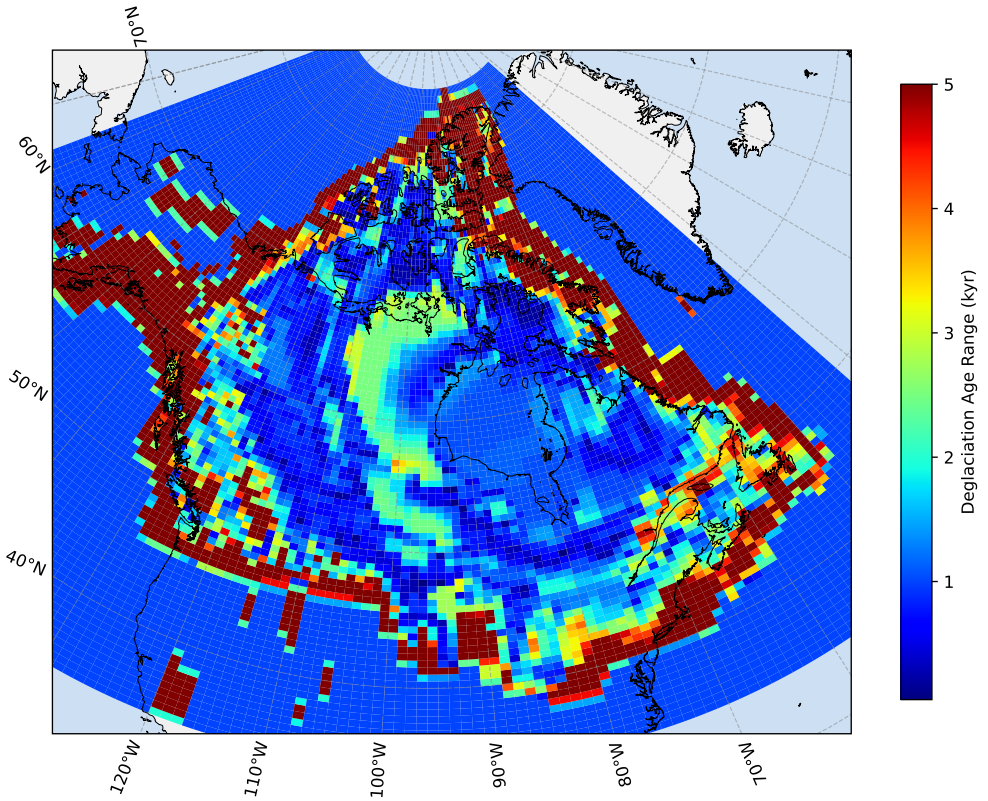


Figure S2: **Range of predicted deglaciation age for the prior ensemble of ice sheet reconstructions.** For each grid cell, the deglaciation age range is the difference between the minimum and maximum age predicted by any of the reconstructions.

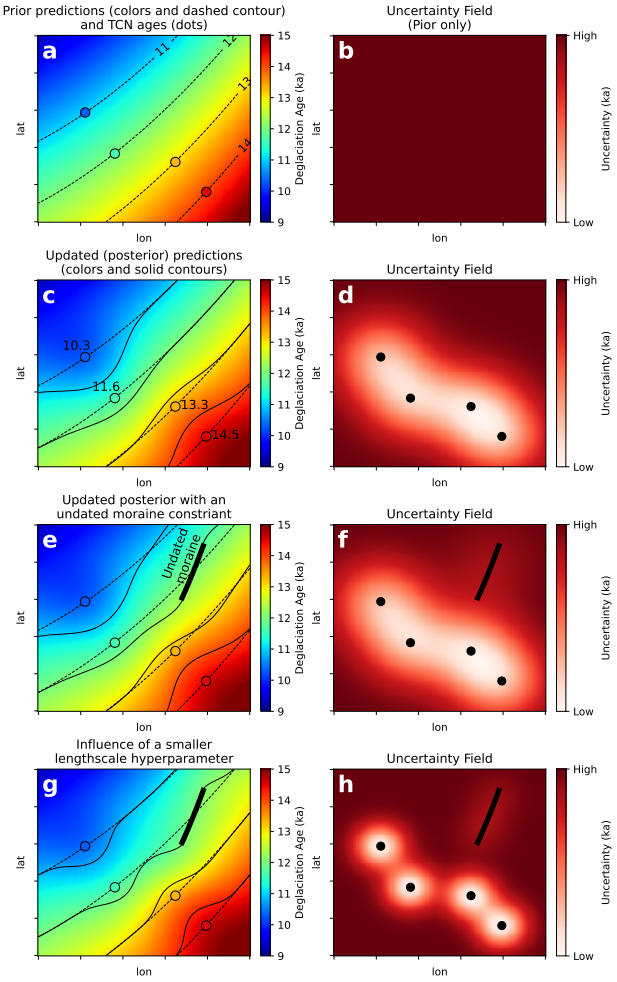


Figure S3: **Illustration of the Bayesian statistical approach.** Note that this visual is schematic and does not reflect an actual Bayesian inversion. (**A**) Prior field of deglaciation time (color scale) and selected margins (dashed lines). Colored circles show observations (TCN ages) that differ from the prior. (**B**) Uniform uncertainty field corresponds to the prior estimate before information from the observations is included. (**C**) Updated posterior estimate of deglaciation age (color scale and solid contours) given the observations. The age field is modified near the data to fit the known ages, but resembles the prior where no ages are available (e.g., upper right). (**D**) Associated uncertainty field showing reduced uncertainty near the observations. (**E**) Posterior deglaciation field and margins (color scale and solid lines) updated with an undated moraine (thick black line). The moraine warps the margins to match its geometry, and has a minor impact on the posterior uncertainty (**F**). (**G**) Same posterior estimate as in (**E**) but with a smaller length scale hyperparameter. The spatial impact of each data point is smaller, and the posterior more closely resembles the prior. (**H**) The associated uncertainty field showing generally higher uncertainty due to the shorter length scale.

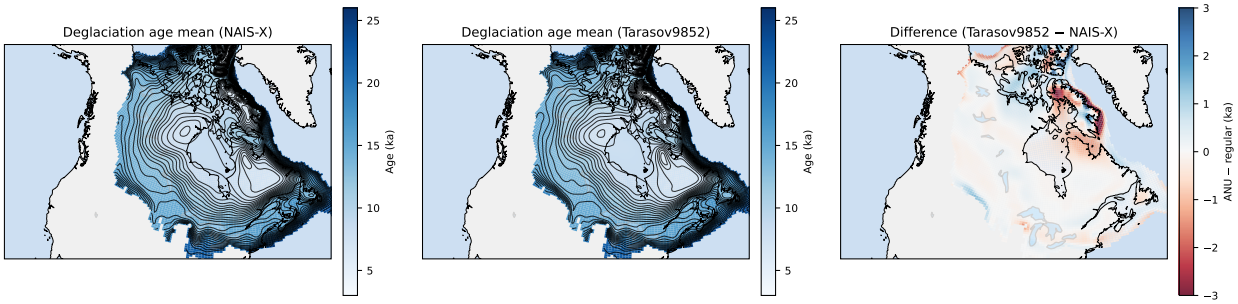


Figure S4: **Sensitivity test of the influence of temporal covariance structure on the inferred deglaciation field.** Left and center panels show the posterior median prediction of deglaciation time for models where the temporal covariance is derived from the NAIS-X reconstruction and '9852' reconstruction from (*87*), respectively. The right panel shows the difference between the two posterior medians.

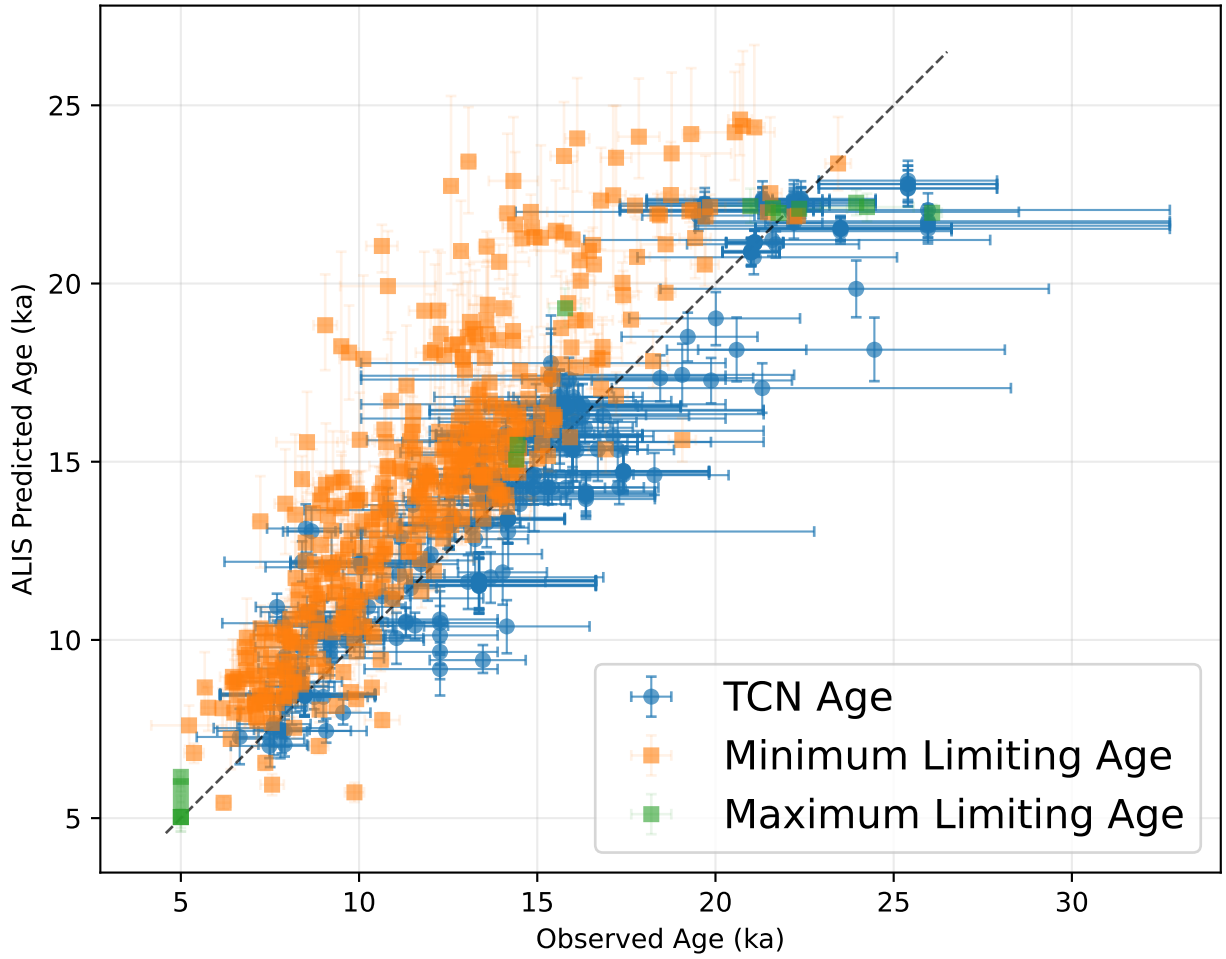


Figure S5: **Posterior predicted ages versus the observed age for geochronological constraints.** Horizontal error bars correspond to the data uncertainties described in 4; vertical error bars correspond to 95% CIs.

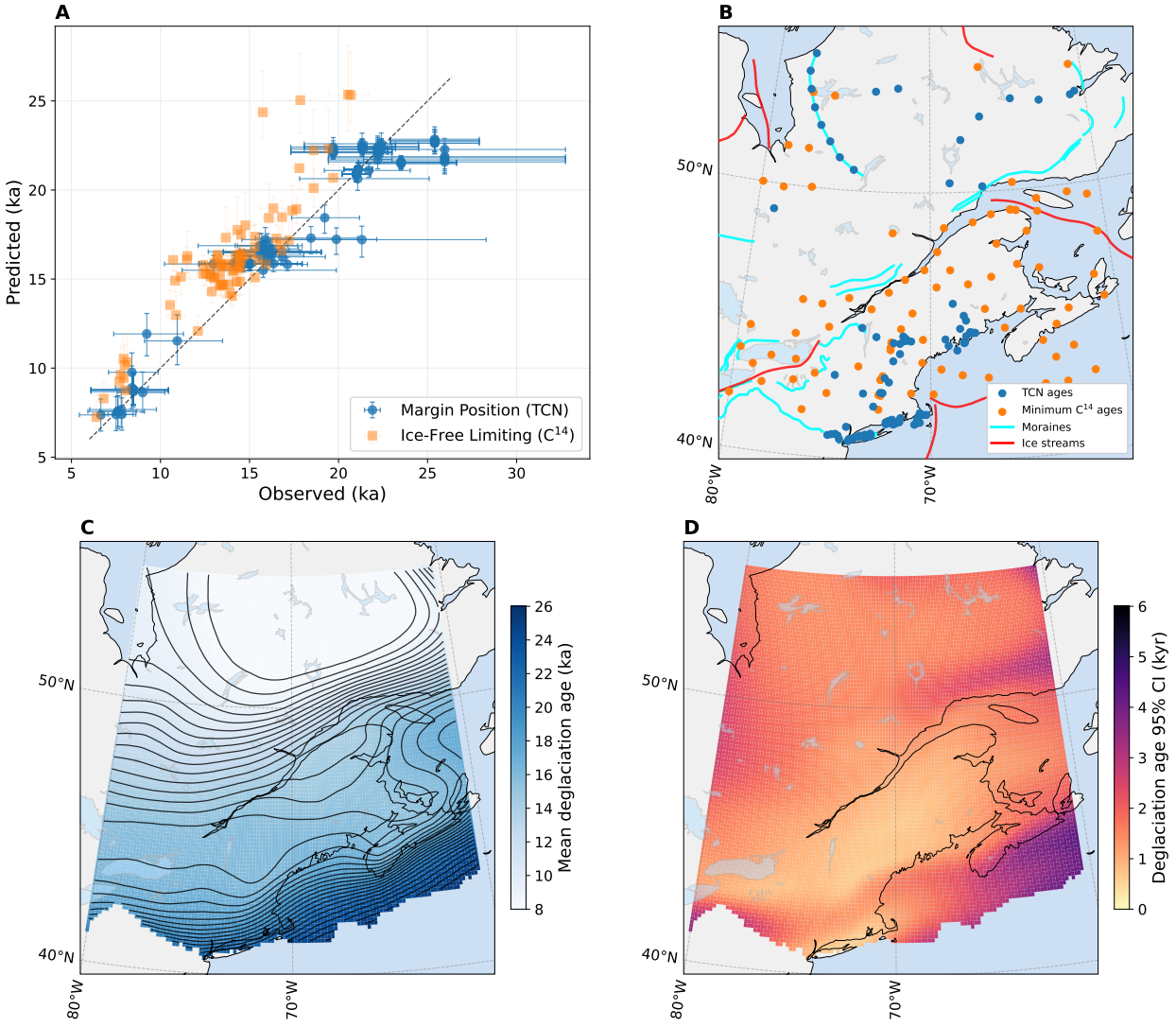


Figure S6: **Input data and results from the regional model.** (**A**) Observed versus predicted ages and uncertainty for the constraints used in the regional model. (**B**) Chronological and geomorphic constraints: TCN ages (blue), C^{14} ages (orange), moraines (black), and ice streams (red). (**C**) Median posterior deglaciation age with ice margins at 0.5 kyr intervals (black lines). (**D**) Deglaciation age 95% CI.

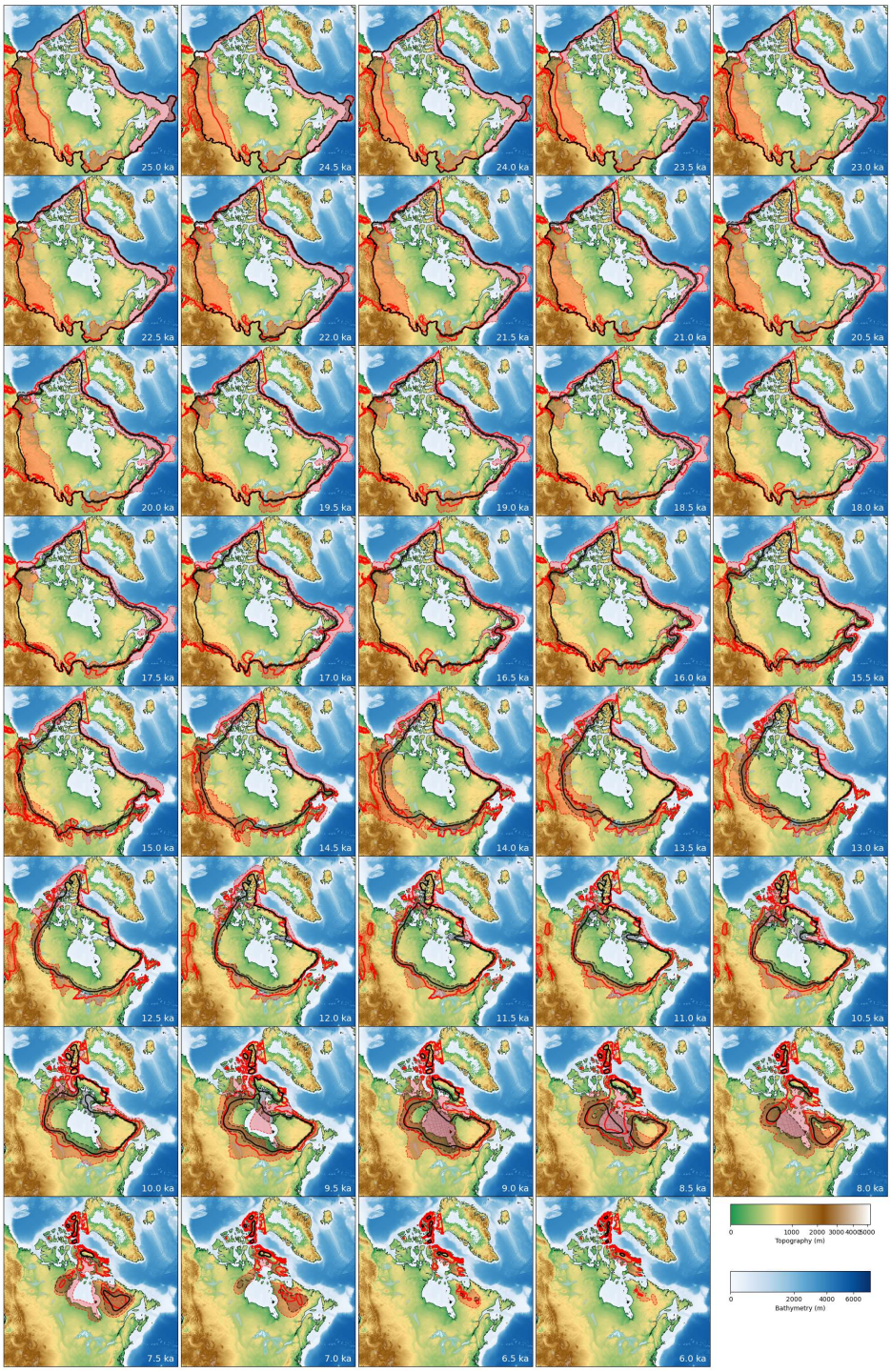


Figure S7: **Comparison between the ALIS and NADI-1 reconstructions.** The black line and grey shaded regions show the ALIS posterior median prediction and 95% CI. The red line and red shaded regions show the NADI-1 optimal and minimum-maximum margins from (*9*) at 500-year time slices. Note, the NADI-1 reconstruction includes the advance to the LGME, while the ALIS places the maximum along the LGM until the initiation of deglaciation. The NADI-1 also includes the CIS, which is not included in the ALIS reconstruction.

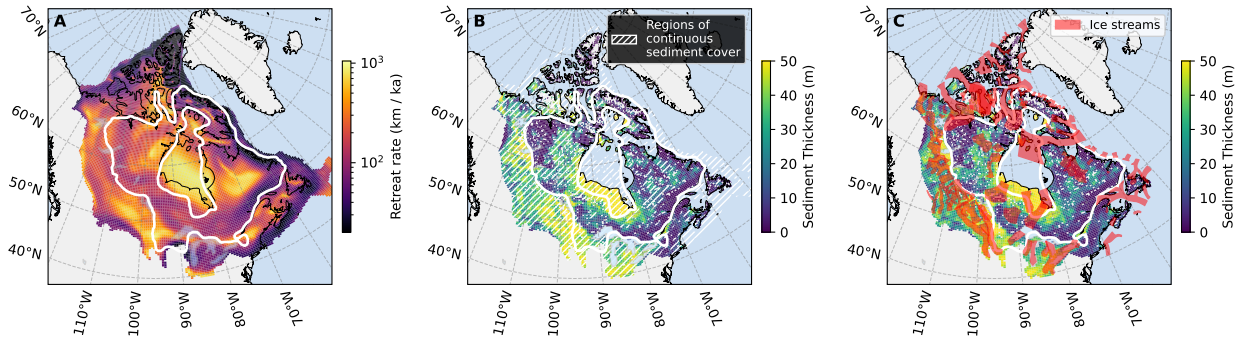


Figure S8: **Predicted retreat rates compared to mapped sediment thickness and ice streams.** (**A**) Average predicted retreat from the ALIS reconstruction; (**B**) sediment thickness (*55*) and regions of continuous sediment cover [white hashes; (*54*)]; (**C**) sediment thickness as in (**B**) and mapped ice streams form (*44*). Thick white line shows the outline of the Canadian Shield for reference.

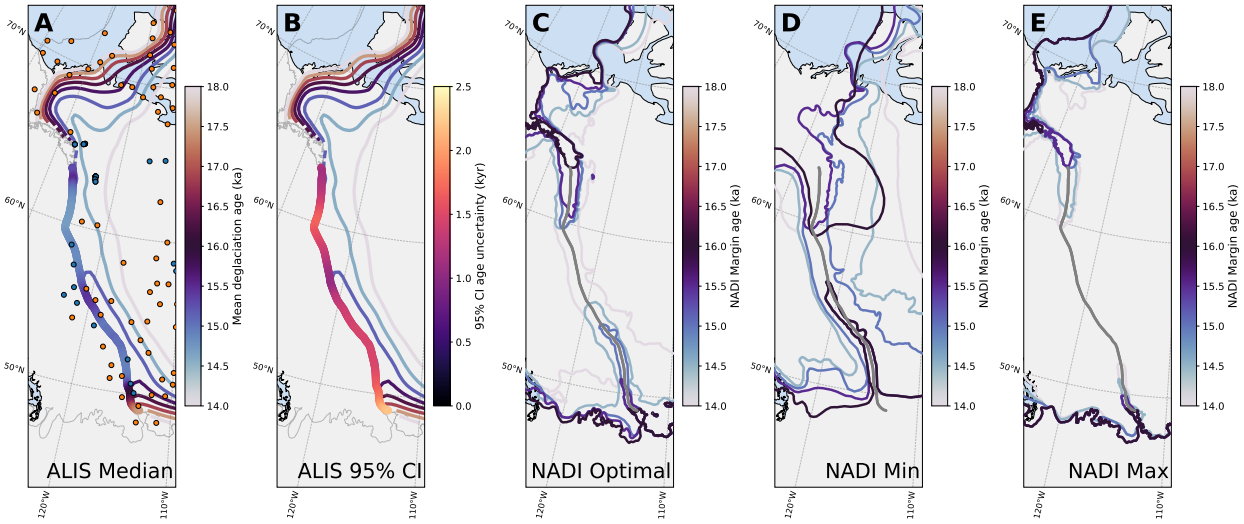


Figure S9: **Estimates for the timing and uncertainty in opening of the ice-free corridor between the LIS and CIS.** (**A**) ALIS posterior median; (**B**) ALIS posterior 95% CI; (**C**) NADI-1 optimal margins (*9*); (**D**) NADI-1 minimum margins; (**E**) NADI-1 maximum margins. Blue and orange circles in (**A**) are TCN and minimum-limiting ages used in the ALIS model and include data from the updated database of (*9*) with key TCN constraints from (*24, 112, 113*). Thin gray line in (**A**) and (**B**) is the LGME from the NADI-1 reconstruction. Background topography and bathymetry from ETOPO2 (*114*).

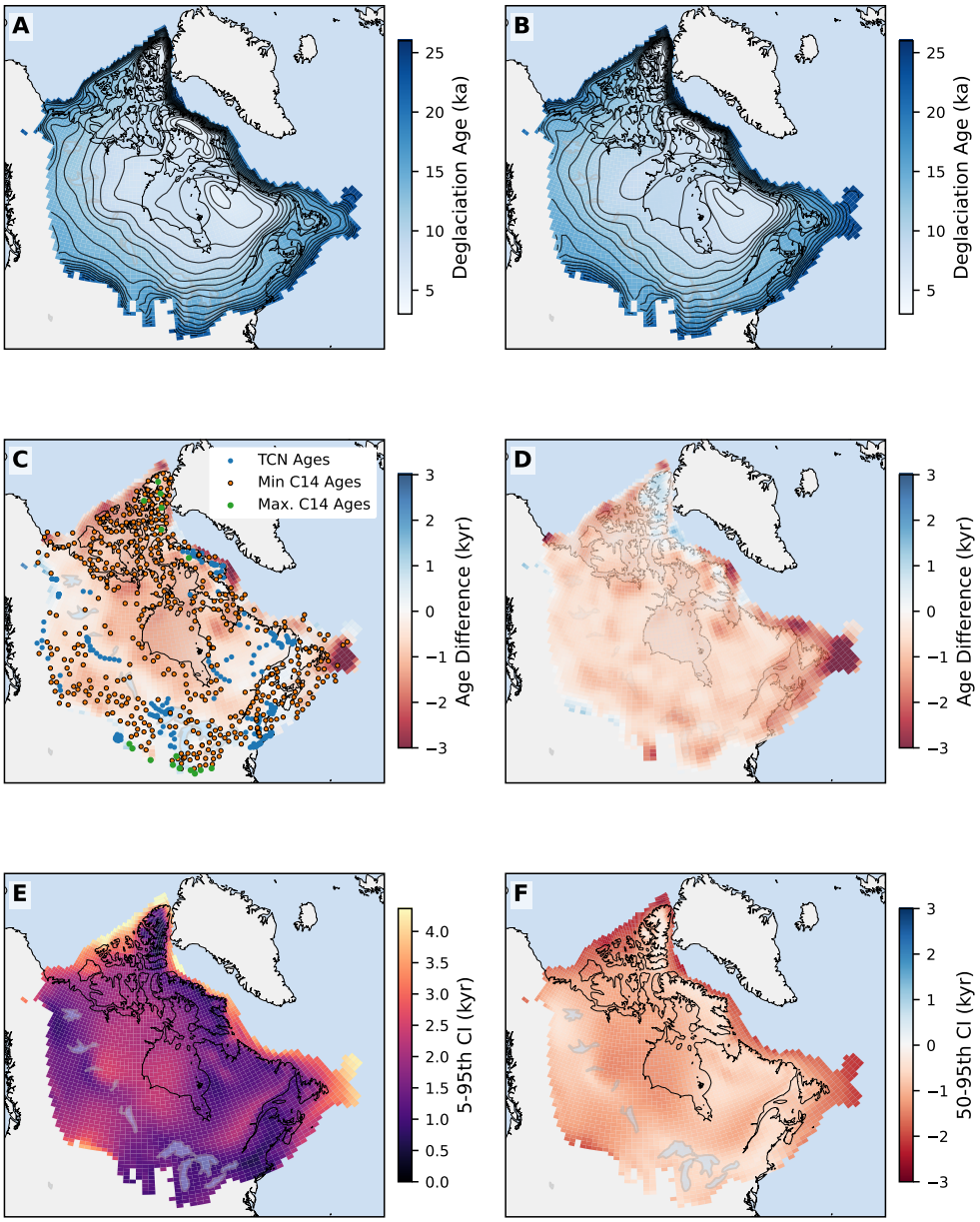


Figure S10: **Model validation experiment results.** (**A**) 'True' deglaciation field; (**B**) reconstructed posterior median; (**C**) posterior bias: difference (**A**) minus (**B**); (D) difference between the 'True' deglaciation field (**A**) and the weighted mean of the ice sheer priors; (**E**) posterior uncertainty (95% CI); (**F**) the high-end uncertainty (50%-95% CI). The posterior bias (**C**) resembles the bias introduced by the inferred GP mean (**D**) and is mostly captured within posterior uncertainty (**F**).

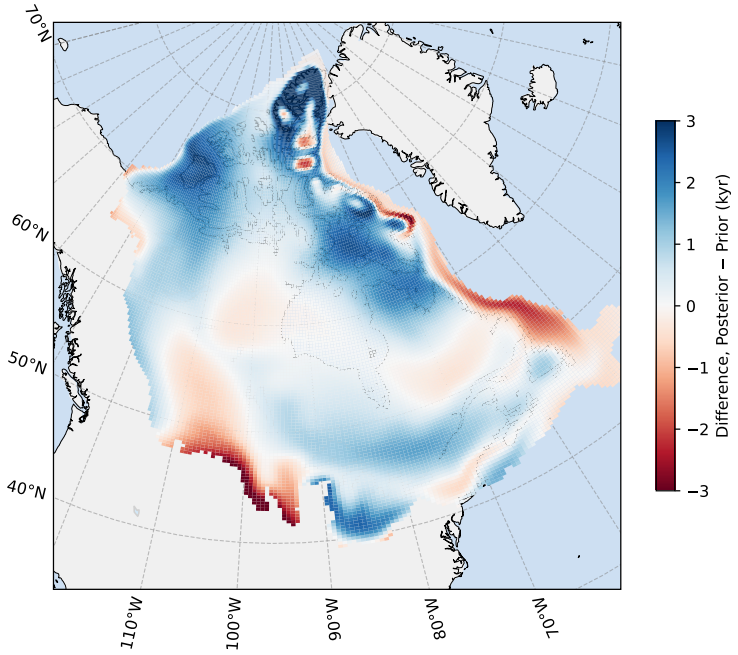


Figure S11: **Bayesian 'prior update', or information gained through sampling and fitting to geologic data.** Color scale shows the difference between the posterior median estimate of deglaciation time based solely on the weighted ensemble of model priors (with global offset, θ_o) and the posterior median estimate of the deglaciation time modeled by the GP (f). The differences illustrate that the Bayesian model must update that field by many thousands of years in places to fit the constraints, i.e., information is gained in this exercise. Areas of no difference (white color) highlight regions where the weighted ensemble sufficiently matches the data, or where no data is available to provide updates.

Caption for Movie S1. Video of the ALIS reconstruction through time (26 to 5 ka). The margin at a given time is the posterior median prediction, as shown in Fig. 2. The color scale along the margin indicates the retreat rate (km/kyr) at that time and location (see section 4). Inset shows the average ice-sheet wide retreat rate through time; the red line indicates the current time being displayed. The black line shows the LGME from (*9*). The Cordilleran Ice Sheet LGME from (*9*) is shown in gray.